Polymer 364 (2026) 130656

Contents lists available at ScienceDirect

Polymer

journal homepage: www.elsevier.com/locate/polymer

From phase structure to mechanical properties: How component selection controls the properties of an amphiphilic polymer conetwork

Hoai Maria Wolschner [a,b], Amin Sadeghpour [c,*], Chieh-Szu Huang [d], Tina Künniger [e], Bernhard Weisse [f], Viviane Lutz-Bueno [g], René M. Rossi [a,b], Luciano F. Boesel [a,**]

[a] Empa, Swiss Federal Laboratories for Materials Science and Technology, Laboratory for Biomimetic Membranes and Textiles, Lerchenfeldstrasse 5, St. Gallen, 9014, Switzerland
[b] ETH Zurich Department of Health Sciences and Technology, Switzerland
[c] School of Food Science and Nutrition, University of Leeds, LS9 2JT, UK
[d] National Tsing Hua University, Function Hybrid Materials Research Group, 101, Sec. 2, Kuang-Fu Road, Hsinchu, 300044, Taiwan
[e] Empa, Swiss Federal Laboratories for Materials Science and Technology, Laboratory for Cellulose & Wood Materials, Überlandstrasse 129, Dübendorf, 8600, Switzerland
[f] Empa, Swiss Federal Laboratories for Materials Science and Technology, Laboratory for Mechanical Systems Engineering, Überlandstrasse 129, Dübendorf, 8600, Switzerland
[g] PSI Center for Neutron and Muon Sciences, PSI, Villigen, 5232, Switzerland

ARTICLE INFO

Keywords:
Amphiphilic polymer conetworks
Mechanical properties
Domain size
Glass transition temperature
Scissor effect

ABSTRACT

Amphiphilic polymer conetworks (APCNs) are thin, flexible and breathable matrices with a heterogeneous nanophase separated morphology, making them ideal candidates for applications such as wearable luminescent solar concentrators (LSCs) for sunlight harvesting. Such materials should possess a well-defined morphology, with domains at the nanoscale that allow the incorporation of luminophores at specific volumes. This improves the efficiency of Förster resonance energy transfer, a feature essential for state-of-the-art LSC systems. Although APCNs have been developed and investigated extensively over recent decades for different applications, we now focus on the specificities of using APCNs for LSCs, and how it influences the design process. We found that the phase ratio of an APCN strongly affects its transition temperature and hence, the extent of its influence on the mechanical properties at room temperature. Similarly, although the chemistry of the hydrophobic domain influences the mechanical properties, the extent of these changes depends on the molecular weights of the precursors. We also demonstrated that Dynamic Mechanical Thermal Analysis (DMTA) a suitable alternative method of investigate in the morphology and phase separation in APCNs for which the phase contrast is too low for small-angle neutron scattering (SANS) and small-angle X-ray scattering (SAXS). In-situ strain SAXS measurements indicated that the macroscopic deformation is reflected at the deformation of the nanoscale domains. Taken together, these results help to design APCNs with tunable morphologies and mechanical properties and suggest alternative characterization methods, which contribute to revealing the full property space of APCNs for applications in energy harvesting and beyond.

1. Introduction

Amphiphilic polymer conetworks (APCNs) are formed from covalently crosslinked hydrophilic and hydrophobic polymer segments, resulting in the formation of distinct nanophase-separated domains. The biphasic architecture enables control over their selective swelling behavior in aqueous and hydrophobic media, mechanical strength and domain size [1,2]. This unique combination of properties has facilitated the expansion of APCNs into a broad range of application areas. The most widely established commercial application of APCNs is in soft contact lenses of silicone hydrogel, in which covalently linked hydrophilic and hydrophobic segments form nanophase-separated [3], optically transparent networks that undergo moderate swelling in water while maintaining elasticity and providing a high level of oxygen

* Corresponding author.
** Corresponding author.
E-mail addresses: a.sadeghpour@leeds.ac.uk (A. Sadeghpour), luciano.boesel@empa.ch (L.F. Boesel).

https://doi.org/10.1016/j.polymer.2026.130656
Received 9 June 2026; Received in revised form 7 August 2026; Accepted 8 August 2026
Available online 10 August 2026

transport [4]. Zhang et al. [5] have reported the design of an anti-biofouling APCN for soft contact lenses, and other fields of application include drug delivery membranes [6–9], biosensors [10–12], biocatalysis [13,14], polymer electrolytes and energy devices [15–18]. APCNs are waterproof, breathable membranes, and are ideal for weather-protective clothing since they are puncture-resistant due to their elasticity and ability to swell in water, enabling self-sealing of the matrix [19].

Since the introduction of APCNs, several concepts have been developed for their synthesis. There are three major types of synthesis strategy [2]: (i) free-radical-induced polymerization; (ii) sequential living polymerization; and (iii) chemical combination of preformed hydrophilic and hydrophobic chain segments. Several recent peer-reviewed studies on APCNs have emphasized that an understanding of their mechanical and morphological properties is crucial in order to optimize their performance. Although the domain size can generally be tuned via crosslinking density, it is primarily governed in APCNs by the molecular weights and chain lengths of the hydrophilic and hydrophobic components [20]. Tsalikis et al. [21] carried out dissipative particle dynamics simulations to demonstrate that the morphology and mechanical properties of APCNs vary strongly with composition, and that different network architectures lead to distinct nanostructures, with direct impacts of the mechanical behavior under strain. Velasquez et al. [22] reported notable enhancements in the Young's modulus and toughness of these materials through hierarchical reinforcement with cellulose nanocrystals and peptide segments. Furthermore, these improvements were found to depend on the phase ratio the APCN and less on the nanoscale morphology. Peptide hydrogen bonding aids in the cellulose nanocrystal dispersion and therefore reinforces the nanostructure. Apostolides et al. [23] highlighted that the tensile strain at break and the swelling capacity of APCNs arise from long-range ordered nanophase-separated domains.

Among the various APCN platforms that have been developed, systems based on poly(dimethylsiloxane) (PDMS) as a hydrophobic phase and 2-hydroxyethylacrylate (HEA) as hydrophilic domain are of particular interest. PDMS provides flexibility, a high level of optical transparency (240-1100 nm), heat resistance, and biocompatibility, due to its chemical inertness. PDMS also enables cost-effective and rapid fabrication of complex microstructures [24]. Here, we present a method for easy and versatile functionalization of hydrophilic poly (2-hydroxyethylacrylate) linked by hydrophobic PDMS [25]. Such PHEA-l-PDMS APCNs are attractive candidates for optical applications, including luminescent solar concentrators (LSCs) [16–18]. In general, the refractive index of an LSC host matrix is ~1.5 [26], to ensure strong internal reflection of the emitted photons. PDMS elastomers have refractive indices of around 1.4 [27], while crosslinked PHEA networks have values of around 1.5 [28], yielding PHEA-l-PDMS APCNs with indices of close to 1.5.

An LSC consists of a transparent waveguide material in which luminophores are embedded. Through photoluminescence, photons that cannot be directly captured by the photovoltaic cell are converted into energies matching the maximum external quantum efficiency (EQE) of the respective solar cell, resulting in an overall improvement in solar energy harvesting. By integrating LSCs, the solar energy is harvested over a large area and concentrated onto a small area, thereby minimizing the numbers of photovoltaic cells required [29,30]. The power conversion efficiency in an LSC is reduced by reabsorption losses arising from the emitted photons being reabsorbed by dye molecules [31]. These losses can be reduced by increasing the Stokes shift between the absorption and emission spectra for the dyes, which can be done using luminophores, as they exhibit large Stokes shifts. However, the host material defines the philicity of the matrix and only luminophores with the same philicity can be applied simultaneously. The biphasic domain structure of an APCN facilitates the simultaneous loading of hydrophilic luminophores into PHEA domains and hydrophobic luminophores into adjacent PDMS domains. APCNs are excellent FRET matrices [16,18]. This enables the creation of Förster resonance energy transfer (FRET) pairs with large Stokes shift, which can be used to obtain LSCs with optimum performance by creating a nanophase-separated scaffold that enables control over the energy transfer [18]. FRET enhances the power conversion efficiency of a LSC by minimizing self-absorption losses [32]. FRET pairs within a critical FRET radius of 2 to 6 nm can be incorporated into APCNs, where 50% of the energy of the donor is transferred to the acceptor for efficient FRET-LSCs [32]. Domain size is a critical parameter in APCNs used for FRET applications due to the strong distance dependence of FRET. Given that FRET efficiency scales inversely with the sixth power of the donor acceptor distance [33], even minor variations in domain size or inter-distance lead to disproportionately large changes in the overall extent of energy transfer. While nano-phase separation with distances smaller than 10 nm is maintained, a key advantage of this system is its ability to accommodate luminophores of different philicities within the same matrix [16,18] to broaden the choice of suitable luminophores. In particular, FRET pairs can be selected that result in the largest possible Stokes shifts, thereby improving the performance of LSCs.

Enhanced control over the morphology and mechanical properties of APCNs is essential to meet the demands of specific applications. The research presented here is aligned with recent advances that have emphasized the importance of understanding the mechanical and morphological properties of APCNs in terms of optimizing their performance. The aim of this study is to investigate the morphology and mechanical properties of APCNs by tailoring the precursor ratios. It explores the impact of hydrophilic domain chemistry and molecular weights of the hydrophobic component to optimize APCNs for luminescent solar concentrator applications, aiming to improve the efficiency of solar cells. The results will contribute to establishing design principles for APCNs for application in LSCs. The use of in situ-strain small-angle X-ray scattering (SAXS) allows for real-time tracking of deformation at both the nano level and the macromolecular scale. Alternative methods are also used to study APCNs for samples with low X-ray contrast in SAXS, low scattering length density difference in small-angle neutron scattering (SANS) or which are too brittle to prepare "dogbone" specimens suitable for tensile testing. Dynamic Mechanical Thermal Analysis (DMTA) data are used to confirm the biphasic network of APCNs based on distinct glass transition temperatures (T_g) for the hydrophilic and hydrophobic domains, thereby providing direct evidence of nanophase separation and microphase immiscibility, while simultaneously characterizing the temperature dependent storage modulus (E′) change.

2. Results and discussion

2.1. APCN synthesis

Hydrophobic and hydrophilic precursors are needed for the synthesis of APCNs (Fig. 1) In these experiments various commercially available substances were tested as hydrophobic precursors, including methacryloxypropyl-terminated poly(dimethylsiloxane) (PDMS) with molecular masses between 4500 [13,16–18,25,34–36] and 25, 000 g mol^{-1}. The long-chain dimethyacrlyate crosslinker 1,12-Dodecanediol dimethacrylate (DDDMTA) was also used as an alternative precursor with low molecular weight. Besides HEA [13,16–18,25,34–36], the influence of the hydrophilic precursor 2-hydroxymethylacrylate (HEMA) was investigated. Furthermore, the hydrophobic acrylate pentafluorophenyl acrylate (PFPA) (PFPA30_70PDMS50, S6) was investigated. The sample is listed in Table 1. PFPA was added, because its active ester groups react with hydrophilic dyes via nucleophilic aminolysis, which enables covalent bonding of the hydrophilic dyes in APCNs.

The protocol used for synthesis in these experiments was based on earlier studies [16,25,34]. The protecting group trimethylsilyl (TMS) was used to temporarily mask the hydrophilic character of the precursor

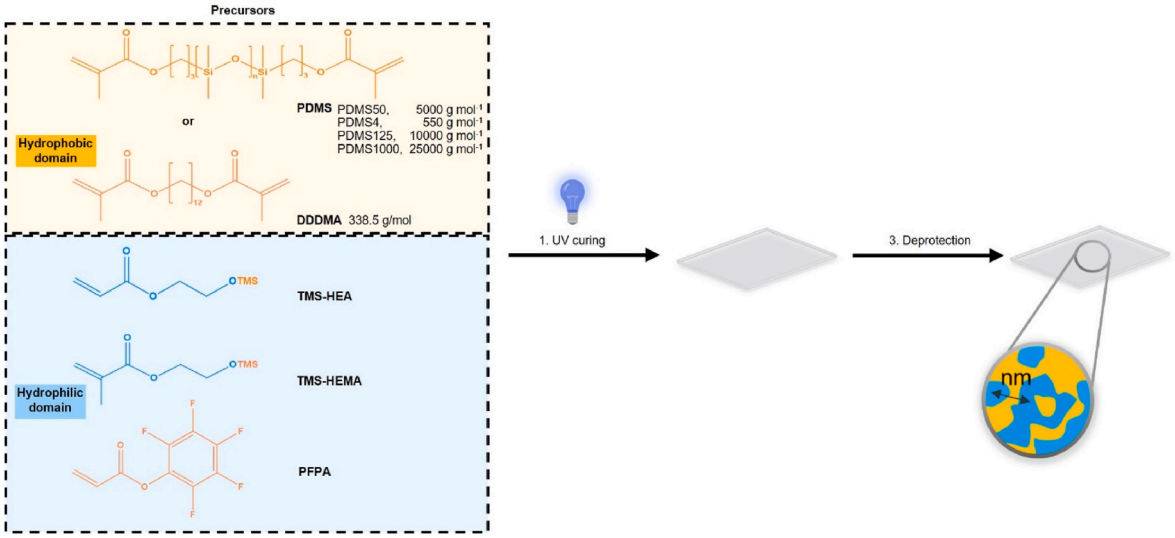

Fig. 1. Synthesis of APCNs via photopolymerization using various hydrophobic and hydrophilic precursors to investigate their influence on the morphological and mechanical properties of the APCNs. As a hydrophobic precursor, either PDMS with different molecular weights or DDDMA were used. Other precursors such as TMS-HEA, TMS-HEMA or PFPA were investigated.

Table 1
Composition of the APCN (with deprotection) and preAPCN (without deprotection) samples.

Sample No.	Sample name[a]	Hydrophob. precursor M_w [g mol^{-1}]	PHEA (wt%)	PFPA (wt%)	PHEMA (wt%)	PDMS (wt%)	DDDMA (wt%)	Irgacure 651 (wt%)	De-protection	X&N[b]
S1	90PDMS50	~5,000	10	-	-	90	-	2	yes	X
S2	87PDMS50	~5,000	13	-	-	87	-	2	yes	X
S3	70PDMS50	~5,000	30	-	-	70	-	2	yes	X, N
S4	63PDMS50	~5,000	37	-	-	63	-	2	yes	X
S5	30PDMS50	~5,000	70	-	-	30	-	2	yes	N
S6	PFPA30_70PDMS50	~5,000	-	30	-	70	-	2	yes	X
S7	PHEMA5_65PDMS50	~5,000	30	-	5	65	-	2	yes	X
S8	70PDMS4	~500	30	-	-	70	-	0.6	yes	N
S9	50PDMS4	~500	50	-	-	50	-	0.6	yes	N
S10	30PDMS4	~500	70	-	-	30	-	0.6	yes	N
S11	70DDDMA	~338	30	-	-	-	70	0.6	yes	N
S12	50DDDMA	~338	50	-	-	-	50	0.6	yes	N
S13	30DDDMA	~338	70	-	-	-	30	0.6	yes	N
S14	70PDMS125	~10,000	30	-	-	70	-	0.6	yes	X
S15	70PDMS1000	~25,000	30	-	-	70	-	0.6	yes	X
S16	70PDMS4no	~500	30	-	-	70	-	0.6	no	-
S17	70PDMS125no	~10,000	30	-	-	70	-	0.6	no	-
S18	70DDDMAno	~338	30	-	-	-	70	0.6	no	-
S19	70PDMS50no	~5,000	30	-	-	70	-	0.6	no	-

[a] For samples denoted as "x hydrophobic precursor type", x indicates the amount of hydrophobic precursor assed. Unless otherwise specified, the rest consists of HEA to a total of 100 wt%, for example, 90PDMS50 contains 90 wt% PDMS50 and 10 wt% HEA. For samples named "other acrylate precursor y_x hydrophobic precursor type", y indicates the amount of the other acrylate precursor added, for example, PFPA30_70PDMS50 contains 30 wt% PFPA and 70 wt% of PDMS50.
[b] Morphology data derived from SAXS (X) or SANS (N).

HEA by forming a trimethylsilyl ether (-OTMS) to ensure the homogeneous mixing of the hydrophilic precursor HEA or HEMA and the hydrophobic precursor. Deprotection was carried out by swelling the preAPCNs overnight in a HCl-acidified mixture of 50:50 wt% water and isopropanol, to remove HEA from the TMS-protection group.

2.2. Strain-induced morphological changes in APCNs

In-situ studies of the changes in the nanodomains were conducted by applying tensile stress to the APCN films while performing SAXS measurements. The samples were subjected to tensile loading at a speed of 5 mm min^{-1} and a strain rate of 3.33×10^{-3} s^{-1}. An exemplary stress-strain curve is given in Fig. 2a with the respective patterns detected in 2D. Stretching the specimen aligns the nanodomains, leading to the formation of anisotropic scattering patterns, which becomes evident in the ellipsoid 2D scattering patterns. Immediately following the breaking point at around 275 s or 90% strain, the domains are reshaped to their original aspect ratio, a finding that emphasizes the elasticity of the nanodomains in this particular APCN sample. Details are reported in section Figure S 1 to Figure S 4.

All the samples investigated here were transparent to visible light indicating the absence of macroscopic phase separation, although at the nanoscopic level, phase separation was evident in the scattering experiments. The presence of a correlation peak at around 0.5 nm^{-1} confirms the domain-domain correlations at the nanoscale present in all samples (Fig. 2b and c and Figure S 2). In the experimental set up, the direction of tensile loading was aligned with the horizontal axis of the detector (q_x), while the transverse direction was aligned with the vertical axis (q_y). Stress was applied at room temperature (RT) and a circular-shaped correlation peak appeared in the 2D scattering image. When exposed to tensile stress, the APCN films gave rise to an ellipsoidal correlation peak in the 2D images, where the peak position was shifted towards

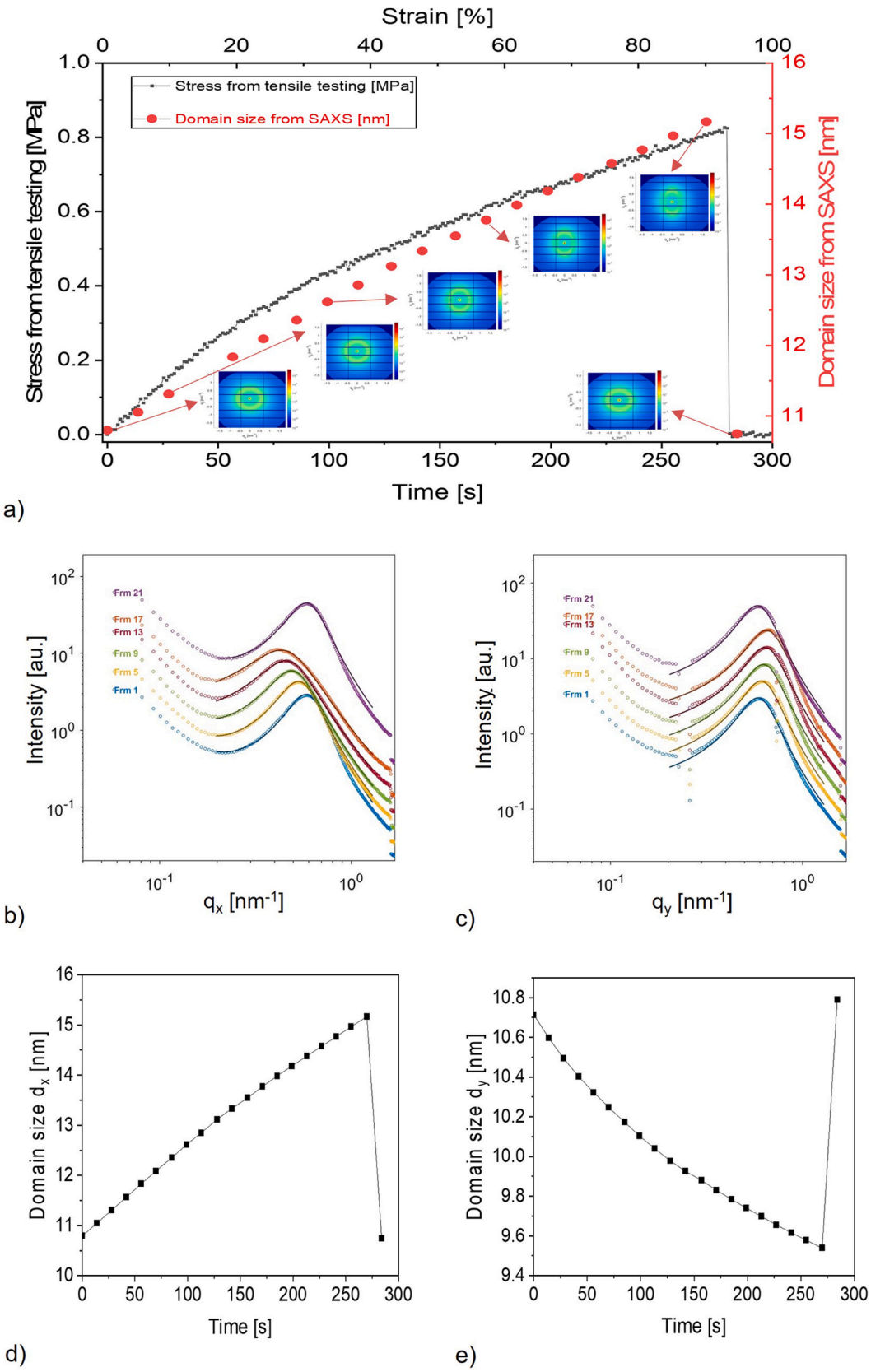

Fig. 2. Real-time strain dependent SAXS measurements to monitor dynamic changes in nanodomain deformation. a) A representative stress-strain curve and corresponding 2D patterns and domain size for sample 70PDMS50 (S3) are depicted. b) SAXS patterns obtained at different time points and integrated azimuthally over a 30° horizontal sector (tensile direction) and c) in the vertical direction. d) Domain size changes during elongation in the horizontal (tensile loading) direction (d_x). e) Domain size changes during elongation in the vertical direction (d_y). f) Quantitative analysis of deformation induced anisotropy in sample 70PDMS50 (S3).

lower q_x values in the horizontal direction (Fig. 2b, Figure S 2 and Figure S 3) and higher q_y values in the vertical direction (Fig. 2c, Figure S 2 and Figure S 3). A high q value corresponds to a large scattering angle, giving a smaller domain size, and vice versa. The ellipsoidal correlation peak in the scattering image indicates anisotropic deformation of structures and their alignment in real space. As a result, during deformation of the nanodomains, the shape is altered to compensate for the imposed external stresses. Nanodomains become elongated along the horizontal tensile direction (Fig. 2d) and their size decreases in the vertical direction (Fig. 2e) during loading. In a study by Wiener et al. [37] in situ SANS was used to link macroscopic stress relaxation with nanostructural recovery in a supramolecular copolymer hydrogel. Following mechanical deformation of the samples, these authors observed the nanodomains to undergo a change in shape, which shifted the position of the scattering peak q. They attributed the stretching of the attached network chains to the generated retractive stress, under which nanodomains are reoriented for stress relaxation [37]. In the APCN samples considered here, it appears that a similar chain-driven nanodomain reorientation mechanism occurs. APCN films containing PFPA (Figure S 2h &k) displayed a broader peak width compared to those containing HEA (Figure S 2a-g, j) or a mixture of HEA and HEMA (Figure S 2i & l). According to the Scherrer equation, which associates the broadening of a correlation peak to the size of an ordered domain, this broadening suggests a short-range ordered arrangement of domains with weak correlation between. A broader peak indicates consistent spacing between the domains is not maintained over a great distance, implying a lower level of ordering for these acrylate phases compared to HEA. This could be attributed to the hydrophobic nature of PFPA, which may lead to a weaker phase separation compared to the much more hydrophilic HEA and HEMA precursors. To provide a quantitative measure of the deformation-induced structural changes, the anisotropy of the 2D SAXS patterns was evaluated by determining the domain aspect ratio d_x/d_y (Fig. 2f), which was plotted against stress. The aspect ratio was calculated from the ratio of the domain size changes d_x during elongation in the horizontal direction (Fig. 2d) and domain size changes d_y during elongation in the vertical direction (Fig. 2e). In the undeformed state (0 MPa), the aspect ratio is 1, confirming a perfectly isotropic morphology. Under tensile deformation, a linear increase in aspect ratio is observed. This trend quantitatively reflects the progressive elongation and alignment of the domains along the tensile direction. At the maximum tensile stress of 0.77 MPa. The aspect ratio d_x/d_y reaches a value of ~1.6, indicating a highly oriented anisotropic domain. This quantitative evolution strongly correlates with the macroscopic mechanical behavior of the material, revealing that the tensile stress directly drives the nanoscale structural reorientation.

Mapping experiments were conducted by scanning a specimen held at 70% of its maximum elongation, using a step size of 0.5 mm. Mapping at different sample positions in the bulk revealed consistency in terms of domain size and ordering across the whole surface area of the specimens (13 mm × 3 mm, Fig. 3a & Figure S 5). The resulting changes in domain sizes in horizontal (tensile loading) (Fig. 3b) direction and vertical direction (Fig. 3c) are mapped in Fig. 3, showing nearly identical values across the scanned area. We confirm that for all investigated samples in Fig. 3 & Figure S 5 the structural integrity of APCNs is maintained at the nanoscale across the surface when they are subjected to a predetermined strain and held at that level, with no differences in regard to nanoscale

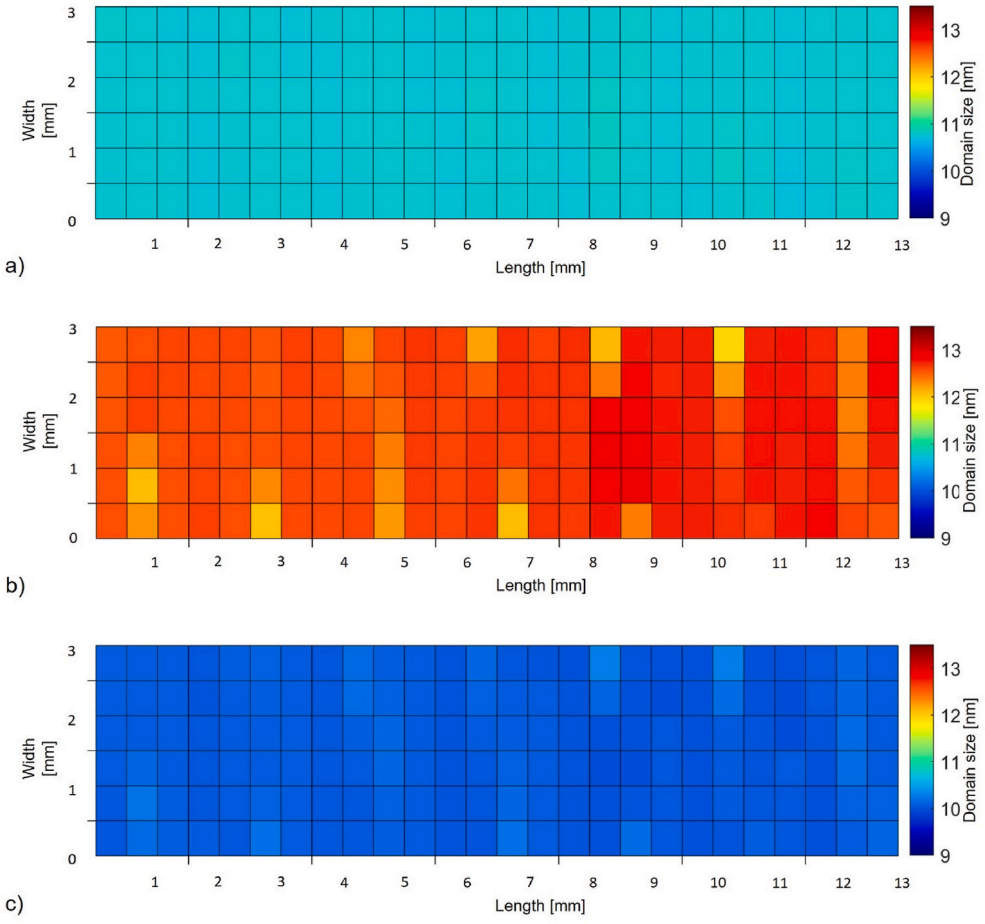

Fig. 3. Mapping of the domain sizes of sample 70PDMS50 (S3): a) in the absence of applied stress, b) in the horizontal (tensile loading) direction, and c) in the vertical (the tensile load is perpendicular to the vertical direction) direction.

reorganization. This points to a homogeneously distributed domain structure and domain response to tensile stress across the whole specimen, despite the random polymerization process.

Following confirmation of the nanostructure homogeneity, the focus of the experiments turned to the stress relaxation behavior of APCNs based on in situ strain SAXS experiments at 7% of maximum strain. Previous work by the current authors [18] has shown that HEA concentrations of around 30 wt% give APCNs that are ideal for LSC applications by achieving domain sizes around 10 nm. Hence, samples 87PDMS50 (S2) (Fig. 4& b) and 70PDMS50 (S3) (Fig. 4c and d) were exposed to a stress of 0.56 MPa at a speed of 5 mm min^{-1} until a strain of 36% was reached (yellow area, I). The strain was held constant (red area, II) for a period of ~840 or ~2340 s (Fig. 4a and c). Immediately after the strain was applied, an exponential reduction in stress was observed. When a polymer is suddenly stretched, its chains become more ordered and aligned, which lowers the entropy [38]; over time, the stress continues to drop at a slower rate (red area, II), while the chains return toward a more disordered state by relaxing and recoiling. Finally, a plateau is reached, where no additional stress relaxation takes place, due to the crosslinked network structure that maintains stability without significant further relaxation. In these experiments, a plateau was not observed within the studied time frame. Sample 70PDMS50 (S3) showed greater step strain than sample 87PDMS50, with the APCN film undergoing fast initial relaxation, followed by less contraction, in which the chains recover their equilibrium disordered state.

2.3. Effect of phase ratio

The morphology of an APCN can be tuned to the desired scale by adjusting the phase ratio [18,35]. In these experiments, the focus was on changing the phase ratio for several APCNs to tune the morphology of the nanodomains and to investigate the mechanical properties. The aim was to obtain controlled domain dimensions that would lead to high FRET efficiencies if two dyes were to be added. The data obtained here reveal distinct effects from hydrophilic and hydrophobic domains on the APCN morphology. The domain size describes the average center-to-center distance of nanophase-separated domains and was obtained from SAXS. The amount of HEA was varied around 30 wt%, which was found in our previous work [18] to be the best value for applications involving LSCs. An increase in the amount of the hydrophilic phase HEA led to an enlargement of the domain sizes (Fig. 5a), consistent with the findings reported by Fodor et al. [39] for poly (N-vinylimidazole)-l-poly(tetrahydrofuran) conetworks, Wilhelm et al. [40] for crosslinking the hydrophilic PHEA with the hydrophobic poly (2-(1-ethylpentyl)-2-oxazoline) (PEPOx) and Huang et al. [18] and Velasquez et al. [35] for PHEA-l-PDMS APCNs. At higher concentrations the compatibility of HEA with the hydrophobic phase PDMS decreased, thereby driving stronger phase separation, leading to larger domains and hence enlarged interdomain distances. Malo de Molina et al. observed an increase in domain sizes with higher content of the hydrophilic 2-(dimethylamino)ethyl methacrylate (PDMAEMA), for block

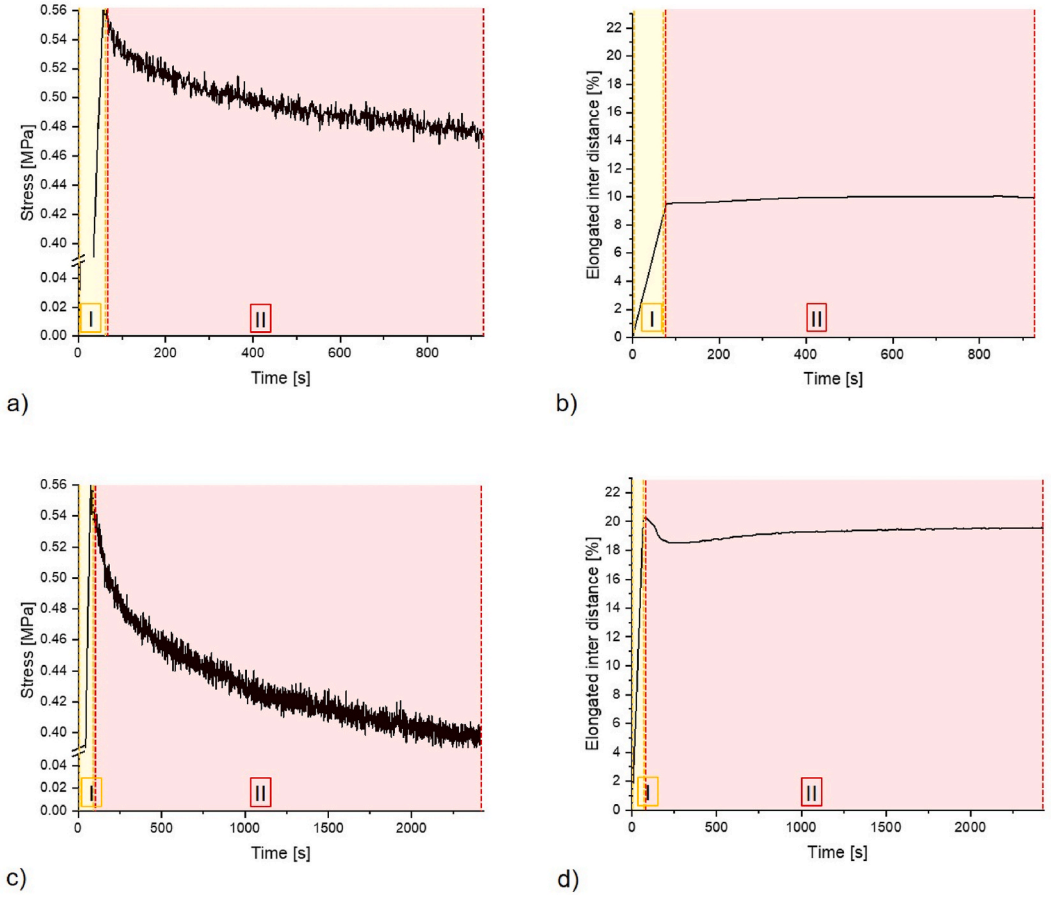

Fig. 4. Stress relaxation behavior of sample 87PDMS50 (S2) subjected to a tensile stress of 0.56 MPa until a strain of 36% was reached (yellow area). The strain was held constant (red area), and the resulting stress decay was monitored over a period of 850 s to observe the response at the macroscopic level. The strain was then retracted at a rate of 0.05 mm min^{-1}. b) Nanostructure of sample 87PDMS50 (S2) during elongation and stress relaxation simultaneously. c) Stress relaxation behavior of sample 70PDMS50 (S3) subjected to a tensile stress of 0.56 MPa until a strain of 36% was reached (yellow area). The strain was held constant (red area), and the resulting stress decay was monitored over a period of 2340 s to observe the material's response at the macroscopic level. d) Nanostructure of sample 70PDMS50 (S3) during elongation and stress relaxation. (For interpretation of the references to colour in this figure legend, the reader is referred to the Web version of this article.)

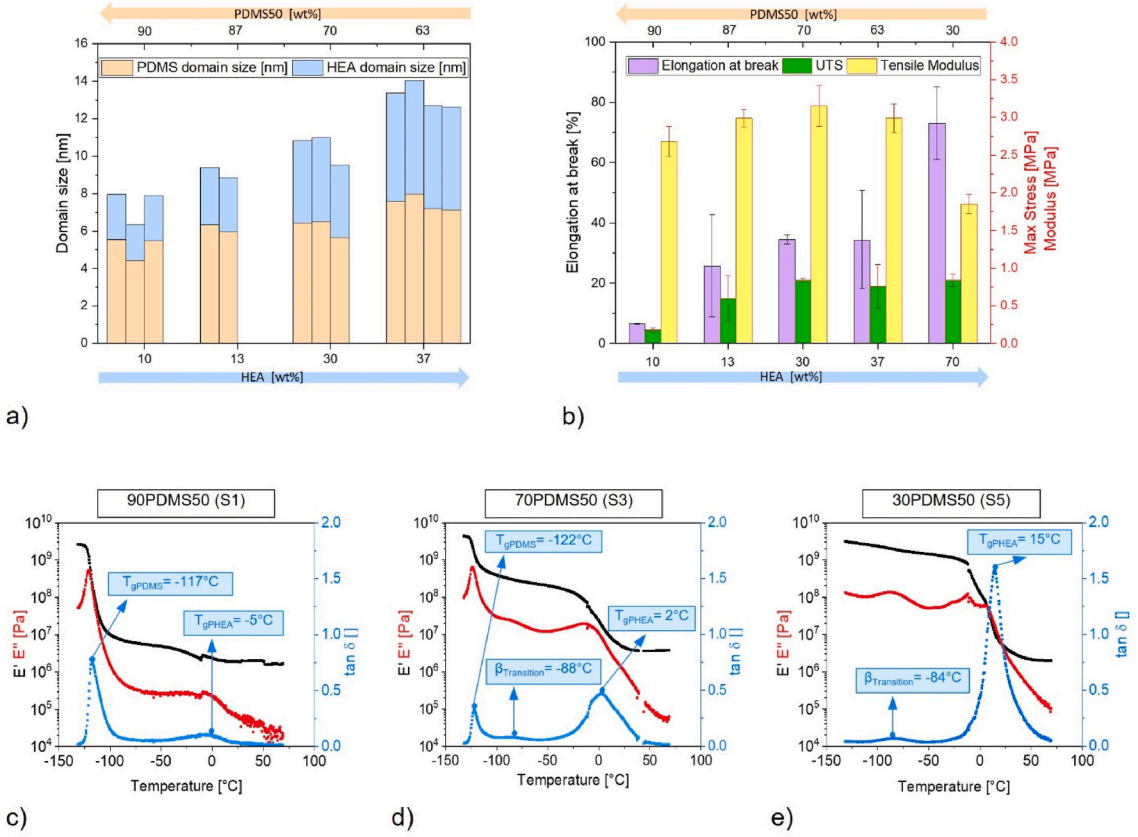

Fig. 5. Domain sizes and individual domain sizes (PDMS shown in orange and HEA in blue) determined for APCNs with HEA weight ratios varying between 10 wt% (90PDMS50, S1) and 37 wt% (63PDMS50, S4). b) Uniaxial tensile testing of APCNs with different HEA ratios depicting elongation at break (purple), ultimate tensile strength (UTS) (green) and the tensile modulus (yellow). c) DMTA temperature sweep of 90PDMS50 (S1), 70PDMS50 (S3) and 30PDMS50 (S5) (from left to right) depicting the storage modulus E' (black), loss modulus E" (red) and tanδ (blue). (For interpretation of the references to colour in this figure legend, the reader is referred to the Web version of this article.)

copolymer APCNs based on hydrophobic methyl methacrylate (MMA) monomer repeating units and the hydrophilic PDMAEMA monomer crosslinked by ethylene glycol dimethacrylate (EGDMA) [41].

A linear relationship was observed between the content of hydrophilic HEA and the inter domain spacing d (Figure S 6). Data were fitted using the equation d = a + b*x and we found that the factors a = 1.15 and b = 0.12 gave the best R^2 with R^2 = 0.93, where the parameter x describes the amount of HEA added in wt%. Inter domain spacing scales linearly with total domain sizes, calculated as the sum of domain sizes of the hydrophilic domain and hydrophobic domain. Here, d = 5.83 + 0.19*x (R^2 = 0.83, Figure S 6).

No continuous trend in the domain aspect ratio is observed when moving from sample 90PDMS50 (S1) to 63PDMS50 (S4) (Figure S 4). Instead, the sample 90PDMS50 (S1) remains almost completely isotropic throughout the entire tensile test. Whereas the samples 87PDMS60 (S2) to 65PDMS50 (S4) all exhibit stress-induced anisotropy. Notably, within this latter group, sample 70PDMS50 (S3) displays a higher sensitivity to stress, with its aspect ratio increasing more steeply.

The effect of the phase ratio of APCNs on their mechanical properties was investigated by exposing samples 90PDMS50 (S1) to 30PDMS50 (S5) (Table 1) to uniaxial tensile stress (Fig. 5b). Elongation at break increases as the amount of HEA in samples 90PDMS50 (S1) to 70PDMS50 (S3) was raised to 30 wt% HEA. When HEA was added at 70 wt%, the strain value showed a two-fold increase compared to lower added amounts of HEA ranging from 13 to 37 wt% (Table S 1). The decrease in stiffness was visible in a decrease in the tensile modulus at 70 wt% of HEA. Tuning of the phase ratio did not seem to influence the tensile properties, except for the samples with a high amount of a single phase – either HEA or PDMS (sample 90PDMS50 and sample 30PDMS50). The glass transition of PHEA is observed in literature at ~37.5°C [42,43] and the material was therefore expected to be in its glassy state. An increase in elongation at break and a decrease in tensile modulus was observed with an increasing proportion of HEA, especially at high HEA amounts; a result that is aligned with findings reported in the literature [35]. This indicates that tensile testing is not an ideal approach to investigating the influence of the phase ratio on the mechanical properties in our systems, as has also been found previously for PHEA-l-PDMS APCNs [35]. Their high standard deviation values indicate significant variability across specimens, highlight challenges related to the method used to test the mechanical properties.

DMTA measurements were performed, which allowed for a study of the viscoelastic properties of polymers as a function of temperature, time and frequency thereby providing detailed insights into the mechanical behavior and transitions of the polymer samples. Due to the biphasic nature of APCNs, two distinct T_g values are expected. In the literature, the value of T_g for PDMS, determined from the tan δ peak with DMTA, has been reported as between −125°C and −114°C [44] for commercial silicone elastomers, and the value of T_g for PHEA has been determined as ~37.5°C [42,43] in the same way. Phase-separated, immiscible polymer blends exhibit two distinct values of T_g, whereas a single value for T_g indicates a homogenous phase arising from miscible polymers. DMTA data not only provide information about the mechanical properties of the material but also offers insight into its phase morphology. In these experiments, two peaks were observed in E" and tan δ (Fig. 5c–e) for samples 90PDMS50 (S1) and 70PDMS50 (S3) (Table 1), thus proving that phase-separated domains were created at the nanoscale, since the

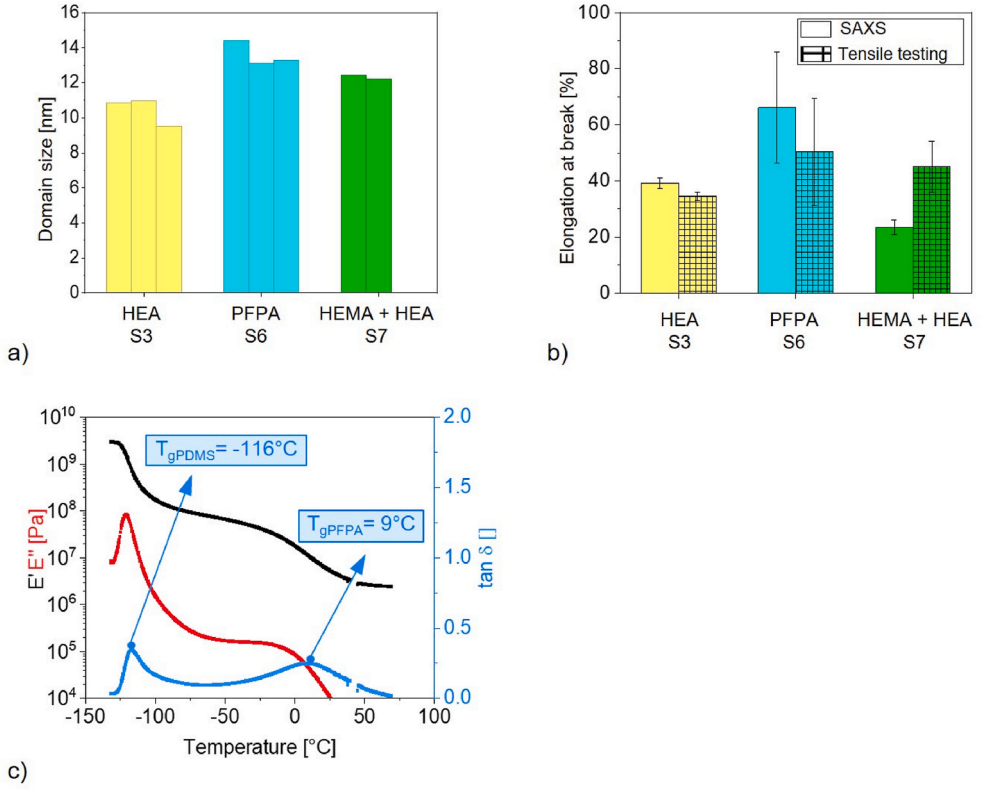

Fig. 6. Effect of the hydrophilic composition on morphology and mechanical properties. a) Influence of the hydrophilic component on domain size for samples 70PDMS50 (S3), PFPA30_70PDMS50 (S6) and PHEMA5_65PDMS50 (S7). b) Elongation at break derived from SAXS- and tensile testing measurements for the same samples. c) DMTA temperature sweep of PFPA30_70PDMS50 (S6) depicting the storage modulus E' (black), loss modulus E" (red) and tanδ (blue). (For interpretation of the references to colour in this figure legend, the reader is referred to the Web version of this article.)

films were transparent, excluding separation at the macroscopic level.

The T_g of PDMS is aligns with the literature value of -117°C [44] of −117°C. However, increasing amounts of the PHEA phase shifted the T_g toward lower temperatures. For sample 30PDMS50 (S5) T_g for PDMS was not visible in the temperature range −130°C to 75°C; the peak position may have been shifted to below −130°C, outside the range measurable with DMTA used in these experiments. Petróczy et al. [45] used DSC to determine the glass transition of their nanophase-separated polystyrene-l-poly(dimethylsiloxane) (PS-l-PDMS) conetworks and observed a slight shift of approximately 4°C towards higher T_g in PDMS as the amount was increased from 59 to 84%. In the present work, a temperature increase of 5°C was observed when the amount of PDMS was increased from 70 wt% to 90 wt% (Fig. 5c and d). This shift is relatively small compared to the more pronounced decrease in T_g observed for the crosslinked PS component. Compared to the PS homopolymer, T_g has been found to decrease by between 19°C and 40°C depending on the amount of PS added to the network [45]. In the current work, a similar shift was observed when using an increasing amount of HEA: a change in peak position towards higher temperatures (Fig. 5c–e) for $T_{g\ PHEA}$ was noticeable for all samples. We observed that the T_g is reduced by 23°C to 42°C compared to the T_g for the homopolymer PHEA at ~37.5°C [42], as the amount for PHEA was reduced from 70 wt% to 10 wt%.

Segmental motion within the interphase leads to shifts and/or asymmetric broadening in T_g [46]. This is supported by the observation of a β-transition peak for PHEA; for samples 70PDMS50 (S3) and 30PDMS50 (S5), this is visible between −88°C and −84°C. The β-transition is a secondary relaxation process, appearing below the T_g that corresponds to the local motion of the polymer backbone; it is smaller than the large-scale motions of long chain segments that occur during the T_g [47]. Asandulesa et al. [48] found that in polar-nonpolar polysiloxane co-networks, β relaxation is favored by increasing the amount of polar groups. The β-transition may not be visible for the APCN sample 90PDMS50 (S1) tested here because the amount of the PHEA phase is probably too low. Another possible explanation is that the β-transition is hidden by the strong T_g peak for PDMS.

The domain size for PDMS shows only minor variations with a change in phase ratio, whereas for HEA, it increases more with higher HEA content (Fig. 5a). Fodor et al. [49] studied amphiphilic poly(*N*-vinylimidazole)-*l*-poly(tetrahydrofuran) (PVIm-l-PTHF) conetworks and demonstrated that the extent of the variation in T_g depends not only on the composition but also on the molecular weight of the PTHF component. This indicates a "scissors effect" where the macromolecular crosslinker functions as scissors and the glass transition temperature of the comonomer chain segments is solely determined by the length of the segment between consecutive crosslinking points M_c, rather than by the entire chain length. The value of M_c for the PHEA segments can be calculated as follows [2,48,49]:

$$M_c\left[g\,mol^{-1}\right] = 0.5\,\frac{wt\%_{HEA}}{wt\%_{PDMS}} M_{PDMS}\ \left[g\,mol^{-1}\right] \quad (1)$$

Where $wt\%_{HEA}$ and $wt\%_{PDMS}$ represent the weight percentages of HEA and PDMS, and M_{PDMS} is the average molecular weight of PDMS. The M_c values for 90PDMS50 (S1), 70PDMS50 (S3) and 30PDMS50 (S5) are 278, 1071 and 5833 g mol^{-1}, respectively. The average molecular weight between crosslinks M_c is inversely proportional to the crosslinking density [50]: the more HEA is added, the lower the degree of crosslinking. This also explains the stress relaxation results (Fig. 4a and c). Consequently, sample 70PDMS50 (S3) (Fig. 4c) relaxes faster compared to 87PDMS50 (S2) (Fig. 4a), exhibiting a steeper initial drop in stress once the strain is held constant. This behavior is driven by differences in Mc values (Table 2), as the E-Modules of the samples at

Table 2
Average molecular weights between crosslinking points M_c for PDMS precursors with different molecular weights and DDDMA.

Sample name	Molecular weight of the hydrophobic phase [g mol^{-1}]	M_c HEA [g mol^{-1}]
70PDMS4 (S8)	~500	107
70PDMS50 (S3)	~5,000	1071
70PDMS125 (S14)	~10,000	2,143
70PDMS1000 (S15)	~25,000	5,357
70DDDMA (S11)	338	73
90PDMS50 (S1)	~5,000	278
87PDMS50 (S2)	~5,000	374
63PDMS50 (S4)	~5,000	1,468
30PDMS50 (S5)	~5,000	5,833
50PDMS4 (S9)	~500	250
30PDMS4 (S10)	~500	583
50DDDMA (S12)	338	169
30DDDMA (S13)	338	394

room temperature are similar (Fig. 5b).

Schroeder and Roland [51] report that in end-linked PDMS networks the α dispersion broadens in response to an increase in crosslinking density. α dispersion represents segmental motion that occurs at T_g; as the crosslinking density increases, these movements become more restricted, which broadens the peak. This effect is in accordance with our findings. Sample 90PDMS50 (S1), with the highest crosslinking density, exhibited the greatest peak broadening, whereas sample 30PDMS50 (S5) had the lowest crosslinking and a sharper peak. A higher degree of crosslinking also leads to a stiffer polymer and an increased modulus. The values of the E' at RT were ~250 MPa [43] for the homopolymer PHEA and 0.4 MPa for PDMS [52].

In accordance with the Flory-Fox equation [53], the value of T_g for a polymer changes with its molecular weight. A higher molecular weight reduces the free volume, which restricts chain motion and therefore increases T_g, making the polymer stiffer at lower temperatures. According to the scissors effect, this would lead to a decrease in T_g, as observed here (Fig. 5e–c): while the T_g for PHEA remains below RT for all three samples, it lies above RT for the homopolymer. Hence, at RT, the material was in a rubber-like state, regardless of how much of the stiff HEA monomer was added, and the storage modulus for each of the samples S1, S3 and S5 is similar (Table S2). DMTA confirms that RT falls directly within the T_g region of the hydrophilic PHEA matrix. In this transitional regime, the polymer has not reached the stable rubbery plateau and resides on the steepest gradient of the E′ curve. Consequently, the mechanical properties exhibit an extreme sensitivity to the environment; minor fluctuations during tensile testing induce drastic shifts in molecular segmental mobility, translating directly into a significant experimental scatter in the tensile data (Fig. 5b).

The samples reach a rubbery plateau region at ~50°C with E′ values between ~1.6 and 3.6 MPa. The glassy region of the storage modulus (shown in black in Table S2) between the T_g for PDMS and PHEA increases with the content of HEA. Only the influence of PHEA on the APCN film is visible here as it lies below the value of T_g for PHEA. The DMTA results confirm our initial hypothesis that increasing the HEA content of the conetwork leads to the formation of stiffer APCNs, but this effect appears only if HEA is in a glassy state. For instance, at −50°C, a 300-fold increase in the storage modulus is obtained by increasing content of HEA by a factor of only seven times (Fig. 5c–e) and Table S2). The DMTA experiments and the presence of the "scissors effect" demonstrate that tensile testing is not ideal for assessing the influence of the phase ratio on the mechanical properties of these APCNs, as these measurements were performed at RT, which is above T_g for the PHEA in the APCNs due to the "scissors effect". Since both components are in a viscous state at RT, the quasi-static mechanical properties are determined by a complex interplay between the individual mechanical properties, Mc, and domain size.

The findings obtained from tensile testing at RT (Fig. 5b) can be interpreted based on the "scissors effect" in polymer conetworks. The crosslinker serves as molecular scissors that disrupt chain mobility in the crosslinked network. It can be seen that with an increasing proportion of HEA, the average molecular weight between crosslinks M_c increases (Table 2); this leads to fewer crosslinks and hence a higher elongation at break with an increasing amount of HEA.

2.4. *Effect of hydrophilic domain chemistry*

Another essential aspect of APCNs is the influence of the hydrophilic and hydrophobic precursors on hydrophilic domain chemistry, hence on the morphology and mechanical properties of the overall APCN network. Wilhelm et al. [40] studied the hydrophilic acrylates *N*, *N*-dimethylacrylamide (DMA) and HEA, crosslinked by the hydrophobic PEPOx. Although DMA and HEA have similar molecular weights, the domain size for PHEA-l-PEPOx APCNs containing 70 wt% HEA was doubled compared to 70 wt% DMA in PDMA-l-PEPOx APCNs. Consequently, investigation of the effect of hydrophilic domain chemistry on the morphological and mechanical properties of APCNs is therefore crucial for optimization of these properties and materials design. The effect of hydrophilic composition on the domain size was investigated here using HEA (70PDMS50, S3), and a mixture of HEA and HEMA (PHEMA5_65PDMS50, S7) (Fig. 6a). The effect of a further acrylic component on the APCN network was also investigated using the hydrophobic PFPA (PFPA30_70PDMS50, S6). In all three samples investigated here, the PDMS content was 70 wt%. The addition of hydrophobic PFPA to PDMS enlarged the domain size compared to the addition of HEA alone as the hydrophilic phase. When components are more compatible, and therefore better miscible, phase separation is weaker, resulting in smaller domains. This is consistent with the general principle in polymer physics that larger Flory-Huggins interaction parameters indicate poor miscibility and a greater tendency towards phase separation [54]. This describes the thermodynamic compatibility between two polymer components and quantifies the excess free energy of mixing, which arises from the difference in interactions between like and unlike segments. HEA contains a hydrophilic hydroxyethyl group and an acrylate backbone, resulting in structural characteristics that are more similar to PDMS than those of the highly fluorinated PFPA. This similarity means that HEA can easily integrate with PDMS, leading to less pronounced phase separation and smaller domain sizes. For fluorinated acrylate polymers, an increase in the enthalpy of mixing was observed for a higher number of fluorinated repeat units [55]. A higher enthalpy of mixing promotes phase separation, resulting in larger domain sizes, as the components prefer to minimize contact with each other. An increase in the inter domain distance was also observed upon the addition of a mixture of HEA and HEMA.

SAXS measurements were conducted to measure the nanoscale deformation of the domains, while for precise deformation measurements at the macroscale, values for the elongation at break were derived from uniaxial tensile testing, in which strain control was achieved via a laser extensometer. The results for samples containing 30 wt% HEA (70PDMS50, S3) (yellow) and 30 wt% PFPA (PFPA30_70PDMS50, S6) (turquoise) showed that the nanodomains and the bulk material deformed in a similar way (Fig. 6b). When a mixture of HEA and HEMA (PHEMA5_65PDMS50, S7) (green) was used for the hydrophilic phase, the elongation at the nanoscopic level did not translate directly to stretching at the macroscopic level (Fig. 6b). HEMA contains a methyl group attached to its backbone, which is responsible for the inter- and intrachain hydrogen bonds formed between polymeric hydroxyl groups [56]. This, together with the steric hindrance induced by the additional methyl group on the HEMA backbone, stiffens the hydrophilic phase and restricts the chain mobility, making the hydrophilic nanodomains less ductile. In contrast, when HEA is used alone as a hydrophilic phase, greater elongation is visible at the nanoscale due to its higher ductility. The macroscopic elongation at break depends more strongly on the

global network structure than the elongation limits of individual nanodomains, giving it similar deformation values as when HEA (70PDMS50, S3) is used alone.

At equivalent stress levels, samples 70PDMS50 (S3) and PHEMA5_65PDMS50 (S7) exhibit higher domain aspect ratios than sample PFPA30_70PDMS50 (S6), indicating greater development of structural anisotropy under tensile load (Figure S 4). Notably, utilizing a different acrylic component modifies the resulting domain aspect ratio. Despite the variation in their formulation, samples 70PDMS50 (S3) and PHEMA5_65PDMS50 (S7) display similar nanoscale deformation behavior. This is directly attributed to their composition, as sample S3 contains 30 wt% of HEA, whereas sample S7 incorporates only 5 wt% of PHEMA.

At RT the values of the median storage modulus are similar when HEA (70PDMS50, S3) (Fig. 6c) or PFPA (PFPA30_70PDMS50, S6) (Fig. 6c) (Table S2) are added. This is due to the "scissors effect" (Section 2.3), which is evident from a pronounced temperature shift in T_g for

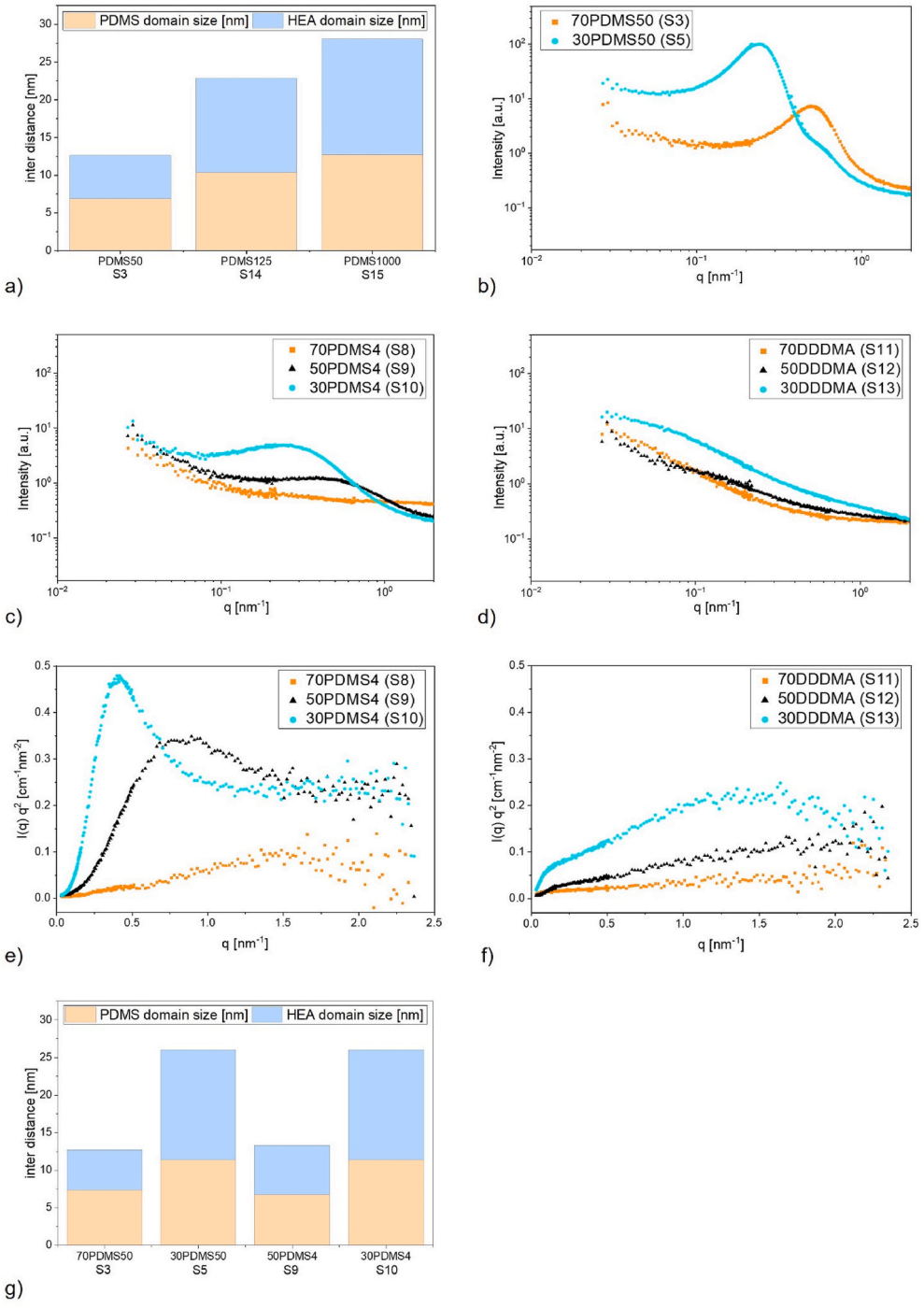

Fig. 7. Inter distances and individual domain sizes for APCNs containing PDMS with different molecular weights of between 5,000 g mol^{-1} and 25,000 g mol^{-1} derived from static SAXS, where all samples contain 30 wt% HEA and 70 wt% of the respective PDMS. Value PDMS50, which has the same composition as our sample 70PDMS50 (S3) was taken from literature [18]. b) SANS results for APCNs containing varying amounts of PDMS50 as the hydrophobic phase. c) SANS results for APCNs containing varying amounts of PDMS4 as the hydrophobic phase. d) SANS results for APCNs containing varying amounts of DDDMA as the hydrophobic phase. e) Kratky plots for APCNs containing varying amounts of PDMS4 as the hydrophobic phase. f) Kratky plots for APCNs containing varying amounts of DDDMA as the hydrophobic phase. g) Inter distances and the individual domain sizes for APCNs containing PDMS50 and PDMS4, derived from SANS.

PFPA. The temperature decreased by 9°C relative to the T_g of the homopolymer ($T_{g\ PFPA} = 55$°C [57]). At RT, the material behaves like an elastic rubber, and adding either HEA or PFPA does not influence the storage modulus (Fig. 6c). At −50°C, below T_g for HEA and PFPA, a higher value for the median storage modulus is found for the sample comprising HEA. HEA contains hydroxyl groups, which can form strong hydrogen bonds. These reduce molecular mobility by restricting the movement of the chains in the network and increasing the binding energy, thereby increasing the stiffness [58–60]. No β-transition was observed for PFPA30_70PDMS50 (S6), unlike for sample 70PDMS50 (S3). The difference between the samples was solely the 30 wt% content of hydrophobic PFPA in sample PFPA30_70PDMS50 (S6) versus 30 wt% of hydrophilic HEA in sample 70PDMS50 (S3). These results are supported by a report in the literature for polysiloxane polar-nonpolar conetworks [48]; where the authors found that a higher polar group content promoted the occurrence of secondary β-relaxation.

2.5. Effect of hydrophobic domain chemistry

Experiments were also carried out to explore the influence of the hydrophobic component on the polymeric network. PDMS precursors with higher molecular weight were selected, and their influence on the inter distance was measured (Fig. 7). The inter distance is defined as the average distance between the centers of nanophase-separated domains. First, the impact of the molecular weight M_w on the domain size was investigated. Fig. 7a, shows the results for samples containing 30 wt% HEA and 70 wt% PDMS with increasing M_w. When M_w is increased from ~5000 g mol^{-1} in 70PDMS50 (S3, Table 1) to 10,000 g mol^{-1} in 70PDMS125 (S14, Table 1) the inter distance also doubles from ~10 nm to ~23 nm, as can be seen from Fig. 7.

In a prior study of block copolymer APCNs based on hydrophobic methyl methacrylate (MMA) monomer repeating units and hydrophilic PDMAEMA monomer crosslinked by EGDMA, the distance remained unchanged regardless of the size of the hydrophobic domains [41]. The authors attributed this to the placement of EGDMA within the center of the linking PDMAEMA block, which reduces its extension, resulting in a partial attachment of PDMAEMA blocks to hydrophobic domains. Furthermore, they proposed that the similar spacing between hydrophobic domains arises because the MMA blocks are half the length of the PDMAEMA blocks, yielding comparable inter domain distances that compensate for structural differences in the block architecture. In the APCN system studied here, however, this behavior could not be observed, as the hydrophobic PDMS precursor is substantially longer, giving rise to a more complex dependence within the network architecture. Fodor et al. [49] synthesized PVlm-l-PTHF APCNs using a PTHFDMA crosslinker with varying molecular weights of between 2,170 and 10,030 g mol^{-1} and reported that a higher molecular weight produced larger inter domain sizes compared to short chain macromonomers. This was attributed to the higher molecular weight crosslinker PTHFDMA, which reduces crosslink density compared to low molecular weight analogs, thereby enhancing polymer segment mobility. In this article, it is proposed that this mechanism also applies to the PHEA-l-PDMS APCN network considered here.

Following the exploration of the impact of PDMS with higher M_w on the APCN network, experiments were conducted to examine the influence of hydrophobic components with low molecular weight, using PDMS4 (~380 to 550 g mol^{-1}) and DDDMA (338 g mol^{-1}). For these precursors, the SAXS measurements did not give a scattering profile with features indicative of a biphasic structure. This lack of contrast is attributed to the similarity in the electron densities of the hydrophilic HEA and the hydrophobic PDMS4 with those of the samples (70PDMS4 (S8), 50PDMS4 (S9) and 30PDMS4 (S10)) and DDDMA with samples (70DDDMA (S11), 50DDDMA (S12) and 30DDDMA (S13)). PDMS4 has around one to two repeating -Si(CH_3)$_2$)O- dimethylsiloxane units, and the composition is dominated by CH_2 groups, making it chemically similar to HEA. The same issue affects DDDMA, as it consists mainly of hydrocarbon groups. Another hypothesis was that phase separation was absent. To investigate our hypothesis, SANS measurements of films soaked in D_2O were performed. Since the contrast in neutron scattering arises from the nuclear scattering length density, rather than from electron density, the scattering contrast is enhanced by swelling the sample with D_2O and the background incoherence is reduced. This selective swelling enhances the neutron contrast between the swollen hydrophilic domains and the hydrophobic domains, enabling visualization of the nanophase-separated morphology. As a reference, the samples S3 (70PDMS50) and S5 (30PDMS50) were measured (Fig. 7b) to compare the determined inter distance values (Fig. 7g) with those derived from SAXS (Fig. 5a). Focusing on sample S3 (70PDMS50), a notable discrepancy is observed between the inter-domain spacings (Fig. 7a) derived from dry-state SAXS (~10.5 nm) and hydrated-state SANS (13 nm) (Fig. 7g). While this 19% increase in d-spacing is traditionally attributed to network expansion, a purely isotropic physical displacement of the domain centers would require a near-doubling of the local network volume. This geometrically overpredicts the more modest matrix expansion constrained by the gravimetric swelling data (Fig. 8a). Instead, this variance highlights a profound shift in the scattering contrast landscape between the two techniques. In the dry state, SAXS resolves the electron density contrast of the phase-separated PHEA domain cores, remaining largely insensitive to the diffuse, mixed polymer interphase between PHEA and PDMS domains. Upon hydration, D_2O selectively imbibes into the hydrophilic regions, including the fuzzy PHEA/PDMS boundary zones. The exceptionally high neutron scattering length density (SLD) of D_2O strongly weights this boundary, effectively broadening the interfacial concentration profile. In phase-separated networks, such an increase in the diffuse interfacial width shifts the dominant thermodynamic fluctuation wavelength (q*) toward lower scattering angles [61]. Consequently, the SANS-derived value of 13 nm represents (Fig. 7g) an *apparent* structural spacing, skewed by the heavily contrasted, expanded boundaries of the hydrated channels, rather than a commensurate physical separation of the underlying covalent crosslinks. For sample S8 (70PDMS4), containing only 30 wt% of the hydrophilic component HEA, no clear peak was measured (Fig. 7c), a finding that is attributed to the poor swelling of the hydrophilic domains in D_2O (see Fig. 8 and associated discussion below). With higher amounts of the hydrophilic phase, a clear SANS peak appears (Fig. 7c) with inter distances of 13 nm for sample S9 (50PDMS4) and 26 nm for sample S10 (30PDMS4). Samples containing PDMS4 and PDMS50 as the hydrophobic phase showed a shift towards lower q values with higher amounts of the HEA phase (Fig. 7c) with larger inter distances (Fig. 7g). This result aligns with those described above (Fig. 5a). Malo de Molina et al. [41] showed that increasing the fraction of the hydrophilic PDMAEMA monomer repeating units decreased, the q values in the SANS profile, resulting in an increase in inter distance. For all the samples tested here, a higher HEA content resulted in visibly increased inter domain spacing (Fig. 7g), indicating a clear phase separation. With PDMS50, distinct SANS features were detected at 30 wt% of HEA (Fig. 7b). A result that may be linked to the lower average molecular weight between crosslinks M_c for S8 (70PDMS4) compared to S3 (70PDMS50) (Table 2); resulting in a higher crosslinking degree for PDMS4, which could restrict the penetration of D_2O into the network, leading to a lower scattering contrast and weaker scattering intensities. In contrast to the samples containing PDMS4, no correlation peak q_{max} was detected within the measured range for samples containing DDDMA (Fig. 7d). To highlight the structural features of the signal, Kratky plots (I (q) q^2 vs q) of samples containing PDMS4 (Fig. 7e) and DDDMA (Fig. 7f) were generated, in which we note the formation of broad peaks. Note that Kratky-plots typically exhibit a slight shift toward higher q compared to plots of I vs q. Kratky plot for sample 70PDMS4 (S8) (Fig. 7e) exhibits a more pronounced peak that was previously subtle in the SANS plot (Fig. 7c). This aligns with the structural trend, in which an increase in the HEA component leads to a decrease in the q-value. Analysis via Kratky plots suggests that in sample 30DDDMA (S13), the

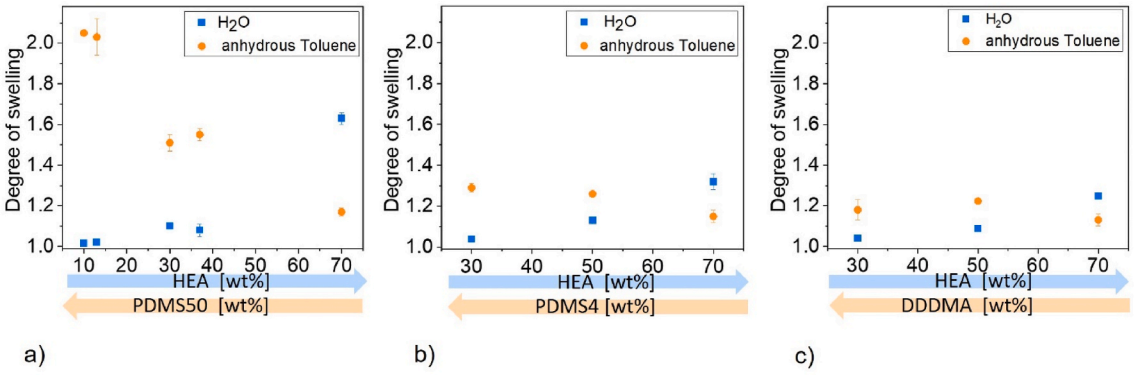

Fig. 8. Results of gravimetric swelling experiments with APCNs swollen in hydrophilic and hydrophobic environments. a) Samples 90PDMS50 (S1) to 30PDMS50 (S5) swollen in water and anhydrous toluene. b) Samples 70PDMS4 (S8) to 30PDMS4 (S10) swollen in water and anhydrous toluene. c) Samples 70DDDMA (S11) to 30DDDMA (S13) swollen in water and anhydrous toluene.

high level of HEA is associated with a weak correlation at approximately $q = 0.45\ nm^{-1}$ (Fig. 7d). As the DDDMA fraction increases, this distance likely shifts to even smaller dimensions (high q) due to the higher density of short-chain crosslinks. This indicates that DDDMA creates a tightly interwoven, nearly homogeneous molecular mesh rather than the discrete nanophase-separated domains observed with longer PDMS precursors. The lack of distinct SAXS features for these samples further support this 'molecular composite' model, where the short length of the DDDMA spacer (approx. $q = 1.85\ nm$) prevents the aggregation of HEA into larger, periodic domains, like for PDMS.

These complementary SAXS and SANS analyses provide direct evidence of the selective accessibility of the hydrophilic HEA phase to aqueous solvents. While the SAXS data show that increasing HEA leads to larger inter distances, SANS with D_2O swelling confirms that these hydrophilic domains are sufficiently interconnected for water to penetrate, and to maintain a homogeneous pattern with a clear inter-domain distance. The linear relationship between HEA content and domain spacing (Figure S 6) is not simply a dry-state geometric effect, as observed in SAXS, but reflects a functional hydrophilic channel system.

APCNs undergo swelling in both solvents owing to their amphiphilic nanostructure [25,35]. To characterize this behavior and to corroborate the SANS analysis and discussion above, swelling tests were conducted. The membranes were swollen in either water or anhydrous toluene to prove the amphiphilic nature of the membranes. As reference, samples 90PDMS50 (S1) to 30PDMS50 (S5) were swollen in both environments for comparison (Fig. 8a). In the aqueous medium, the degree of swelling increased with HEA content, whereas the degree of swelling decreased with increasing HEA content in anhydrous toluene. As expected, the films exhibited a higher degree of swelling in water with a higher amount of the hydrophilic phase and less in the hydrophobic anhydrous toluene. This result is supported by the M_c values for samples 90PDMS50 (S1) to 30PDMS50 (S5) (Table 2), which decreased with lower HEA concentrations, consistent with an increase in crosslinking density within the network. A lower M_c corresponds to a higher crosslinking density, which restricts the polymer network's ability to swell. The same behavior was observed for the samples with PDMS4 (Fig. 8b) and DDDMA (Fig. 8c) as the hydrophobic phase. However, for the samples containing PDMS4 and DDDMA, the degree of swelling was less pronounced, as the M_c values of the HEA segments are low for these samples compared to those containing PDMS50 with higher molecular weight (Table 2). This aligns with the molecular weights of the hydrophobic precursors used in this study. These findings corroborate the SANS results, the low M_c (<250) and low M_w (<500 g mol^{-1}) for PDMS4 explain both the lack of scattering contrast and minimal swelling observed, directly corroborating the hypothesis. A similar behavior was observed for the DDDMA samples. In contrast to PDMS4 (Fig. 8b), the swelling degree of the DDDMA (Fig. 8c) samples in toluene and water remained more uniform across all tested composition ratios, regardless of the phase ratio. We attribute this to a tightly interwoven mesh for APCNs containing DDDMA, which is supported by the suppressed scattering features in the SANS data for DDDMA (Fig. 7d).

The Young's modulus was measured via atomic force microscopy (AFM), since the samples were too fragile to be shaped into dogbone geometries for conventional tensile tests. The AFM force volume mode was used to determine the modulus, using randomly selected spots with approximately 400 measurements per spot. In AFM, the applied force and resulting deformation are mainly confined to a very small region close to the surface by a very sharp tip, which presses locally on the surface. This produces mostly compressive, highly localized deformation and the probed volume is therefore small near the surface zone. In DMTA, oscillatory tensile deformation is applied to the bulk sample. Consequently, AFM modulus values are not interchangeable with those from DMTA data or *quasi-static* tensile data. When the molecular weight of the hydrophobic precursor is increased from ~500 to 10,000 g mol^{-1} (70PDMS4 (S8), 70PDMS50 (S3), 70PDMS125 (S14)), the weighted mean modulus decreases (Table 3 and Figure S 7). This is in accordance with the M_c values (Table 2), which increase with the molecular weight of PDMS, an effect that is linked to a decrease in crosslinking density. A lower crosslinking density results in a lower elastic modulus, as fewer crosslinks allow for greater chain mobility and reduce the network's stiffness. Sample 70DDDMA (S11) has a higher weighted mean modulus than samples containing PDMS precursors with higher molecular weight (PDMS50 and PDMS125). This is reflected in the M_c value of 73 g mol^{-1}, which is closer to the value for PDMS4 (Table 2); accordingly, the modules are in a similar range (~10^2 MPa). Consistent with our findings from tensile testing, the data obtained via AFM measurements demonstrate the challenges of determining mechanical properties at room temperature, which is reflected in the high standard deviations. The wide statistical spread in the elastic modulus stems from the AFM tip interaction (tip radius: 2 to 12 nm), which is highly comparable to the characteristic nanoscale domain size of the APCNs. Random scanning across the alternating stiff hydrophilic and soft hydrophobic domains inevitably results in high standard deviations, as the AFM probe captures localized variations in phase composition [62].

DMTA was used to assess APCN phase separation, as alternative method to SAXS, by detecting two distinct T_g values, thus confirming successful nanophase separation between hydrophilic and hydrophobic domains. Samples 70PDMS4 (S8), 70PDMS125 (S14) and 70DDDMA (S11) were therefore deprotected as described. For samples 70PDMS4no (S16), 70PDMS125no (S17), 70DDDMAno (S18) and 70PDMS50no (S19), no deprotection was carried out (Fig. 9). These samples are referred to as preAPCNs. The samples containing hydrophobic precursors with low molecular weight, i.e., PDMS4 (Fig. 9b) or DDDMA (Fig. 9e), only showed one T_g without deprotection within the measured

Table 3
Weighted mean modules obtained with AFM force volume and respective skewness values.

Sample name	Weighted Mean Modulus [MPa]	Skewness []	Molecular weight of the hydrophobic phase [g mol^{-1}]	T_g for the hydrophobic phase [°C]	T_g for HEA [°C]	M_c HEA [g mol^{-1}]
70PDMS4 (S8)	337 ± 391	0	~500	-	77	107
70PDMS50 (S3)	9.3 ± 5.5	0	~5000	−122	2	1071
70PDMS125 (S14)	1.9 ± 2.3	0	~10,000	−117	11	2143
70DDDMA (S11)	167 ± 134	0	338	-	87	73

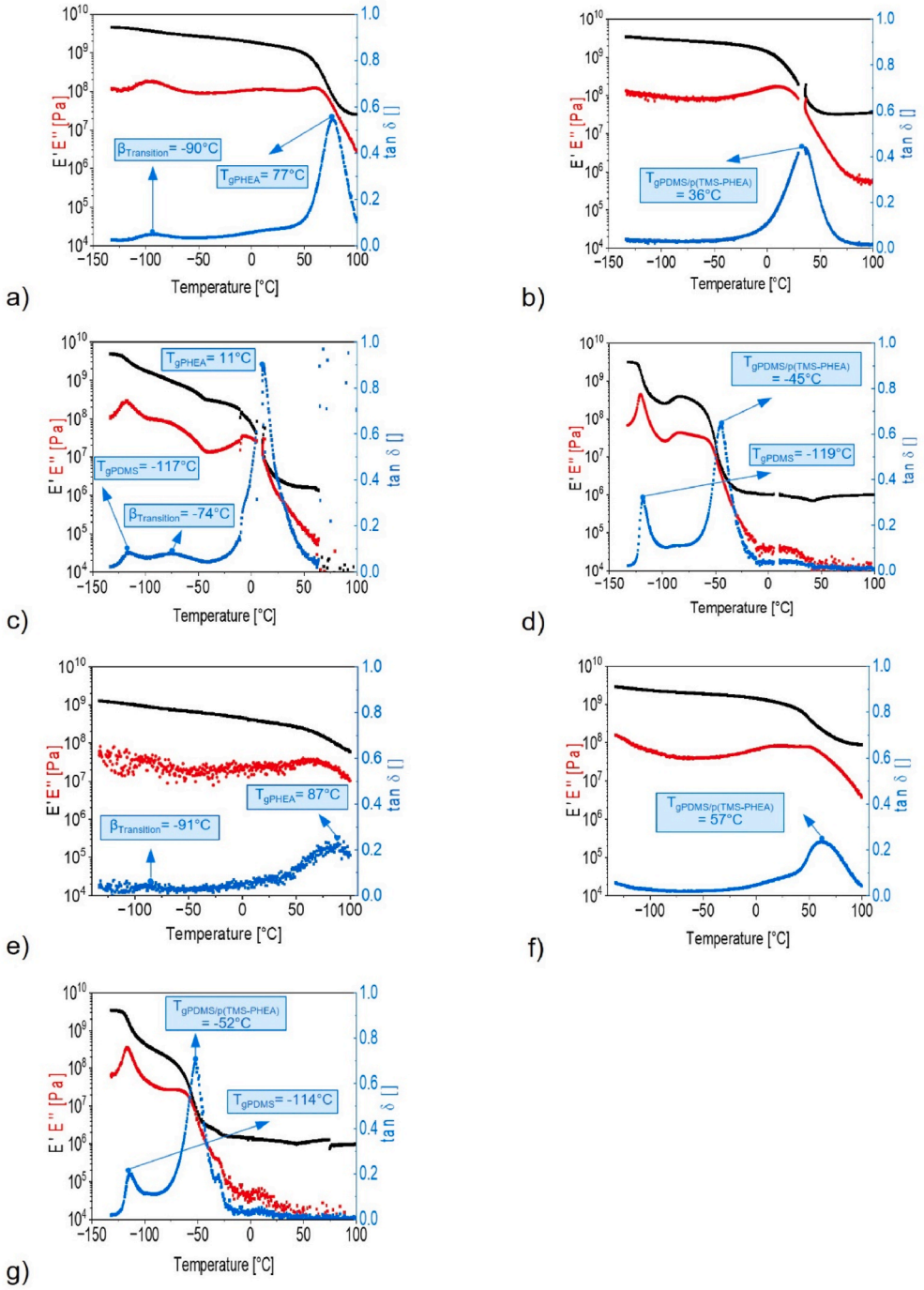

Fig. 9. DMTA curves of the different samples depicting storage modulus (E′, black), loss modulus (E″, red) and loss factor (tan δ, blue). a) Sample 70PDMS4 (S8). b) Sample 70PDMS4no (S16) was not deprotected during the work up. c) Sample 70PDMS125 (S14). d) Sample 70PDMS125no (S17) was not deprotected during the work up. e) Sample 70DDDMA (S11). f) Sample 70DDDMAno (S18) was not deprotected during the work up. g) Sample 70PDMS50no (S19) was not deprotected during the work up. (For interpretation of the references to colour in this figure legend, the reader is referred to the Web version of this article.)

temperature range. Furthermore, the β-transition was only visible in phase-separated networks (Figs. 5d and 9c).

Samples containing PDMS50 or PDMS125 with molecular weights of 5000 or 10,000 g mol^{-1} exhibited two values of T_g within the measured temperature range, both with (Figs. 5d) and Fig. 9c) and without deprotection (Fig. 9g and d). This result is supported by literature [63], showing that T_g reaches a plateau towards −123°C for PDMS with molecular weights higher than 6000 g mol^{-1}. Fox and Flory [53] assumed that chain ends provided additional mobility due to excess free volume. A lower molecular weight elevates the concentration of chain ends, increasing the free volume and reducing T_g. For PDMS with lower molecular weight (Fig. 9a) T_g shifts to lower temperatures as it transitions from a macromolecule to a molecular liquid, making it not accessible with our DMTA device. According to literature, the value is probably around −140°C [63,64]. The same behavior was observed for DDDMA (Fig. 9e) as a hydrophobic precursor, although the T_g for the homopolymer ($T_{g\ DDDMA} = -37$°C [65]) is higher than for the PDMS homopolymer.

For the samples without deprotection, the presence of a single, intermediate T_g was expected, consistent with a miscible system. However, for 70PDMS125no (S17) (Fig. 9d) and 70PDMS50no (S19) (Fig. 9g), two T_g values were observed for the PDMS phase (−119°C and −114°C, respectively) and probably a mixture of PDMS and the p(TMS-HEA) (−45°C and −52°C, respectively), given that the T_g occurs between the respective homopolymers. For the preAPCN samples, 70PDMS50no (S19) (Fig. 9g) and 70PDMS125no (S17) (Fig. 9d), the second T_g peak was ~55°C lower than for the equivalent samples after deprotection, which supports the hyporthesis that this is not the pure T_g of PHEA, but rather a mixture of PDMS and p(TMS-HEA). The preAPCNs prepared with low molecular weight hydrophobic precursors (Fig. 9b) exhibited the same behavior as their high molecular weight counterparts (Fig. 9d & g), displaying T_g at 36°C and 57°C, respectively. These values fall between the T_g of PDMS or T_g of DDDMA and the T_g of PHEA (Fig. 9e). The T_g for the low molecular weight hydrophobic precursors (Fig. 9e) is likely not visible within our experimental temperature range, as demonstrated by the higher molecular weight PDMS precursors (Figs. 5d & 9c). The hydrophobic precursors with low molecular weight (Fig. 9a and e) exhibited higher values for the T_g of PHEA. The molecular weight between crosslinks (M_c) correlates negatively with T_g. As M_c decreases, the resulting increase in density imposes restriction on chain mobility, leading to an elevated T_g. For PDMS4 the temperature shift was ~40°C higher (Fig. 9a). For DDDMA (Fig. 9g) the temperature was ~50°C higher than Tg for the PHEA homopolymer.

As stated earlier, E′ at – 50°C was used for comparison across all samples with adjusted crosslinking densities to determine the influence of the hydrophobic component on the mechanical properties of the respective APCN network. For samples containing PDMS50 or PDMS125 E′ at −90°C were used due to the low Tg of TMS-PHEA. The modulus was higher for samples containing PDMS4 as the hydrophobic precursor (~2.5 GPa, Table S 3), compared to samples containing either PDMS50 (~200 MPa, Table S 2) or PDMS125 (100-400 MPa, Table S 3). For PDMS50 and PDMS125, the modulus values were on the same order of magnitude. Kouakou et al. [66] investigated linear telechelic PDMS precursors with molar masses of between 1,000 and 10,000 g mol^{-1} using nano-indentation. For masses of between 2,000 and 10,000 g mol^{-1}, the modules were on the same order of magnitude, a result that is aligned with the findings presented here. For PDMS with 1,000 g mol^{-1}, these authors found that the modulus was one order of magnitude higher; this is again supported by our results, as the hydrophobic precursors PDMS4 and DDDMA, which both have molecular weights <1,000 g mol^{-1}, where also found to have higher storage moduli than the hydrophobic precursor with higher molecular weight. AFM measurements confirmed the same trend for the modulus as observed with DMTA at RT.

3. Conclusion

In summary, we conducted the factors that affect the morphological and mechanical properties of amphiphilic polymer conetworks (APCNs) for energy harvesting applications. APCN samples have shown that the nanostructural integrity is maintained across the surface when they are subjected to a defined strain, without exhibiting nanoscale reorganization, indicating a homogeneously distributed domain structure, despite the free radical copolymerization process. From in-situ strain SAXS measurements, it was found that the domains adapt to anisotropic deformation through morphological reorganization to compensate for the applied stresses. Macroscopic shape changes are therefore mirrored at the nanoscale, where nanodomains are elongated along the tensile axis and contracted in the perpendicular direction during loading. The nanodomains recover their initial aspect ratio upon strain release, representing elastic behavior. This makes it highly suitable for integration into wearables.

Our results revealed that domain sizes increased due to the interplay between hydrophilic and hydrophobic precursors within the hydrophilic domain chemistry. A higher PHEA content was associated with an increase in M_c, resulting in a lower degree of crosslinking and, attributed to the "scissors effect", in T_g. This finding was supported by our tensile testing results, which demonstrated higher elongation at break with a greater HEA content.

Interestingly, the mechanical properties (e.g., stiffness) remained unaffected by the phase ratio. DMTA measurements revealed that this was due to the APCN network was already in a rubbery state at room temperature. Furthermore, our findings establish DMTA as a viable alternative for characterizing biphasic systems in terms of successful phase separation. In-situ strain SAXS measurements further indicated that domains adapt to anisotropic deformation through morphological reorganization to compensate for the applied stresses. Thus, macroscopic shape changes are mirrored at the nanoscale, The selection and ratio of hydrophobic precursors had a significant impact on both the mechanical and morphological properties of our APCN system. Hydrophobic precursors with a molecular weight of 5,000 g mol^{-1} proved optimal for FRET applications, yielding the desired inter distances. Within the molecular weight range of 5,000 to 10,000 g mol^{-1}, the modulus remained comparable, enabling the fabrication of flexible APCN membranes suitable for integration into wearable solar energy harvesting devices.

These insights are crucial for designing APCN architectures with precise control over phase separated hydrophilic and hydrophobic nanodomains. Such control could enable more efficient LSC systems which facilitate the development of optimized wearable LSCs for solar energy harvesting.

4. Experimental

4.1. Materials

Methacryloxypropyl-terminated poly(dimethylsiloxane) (PDMS, CAS 58130-03-3) with different viscosities of 50-90 cSt (PDMS50, 4,500–5,500 g mol^{-1}), 4-6 cSt (PDMS4, 380-550 g mol^{-1}), 125-250 cSt (PDMS125, 10,000 g mol^{-1}) and 1,000 cSt (PDSM1,000, 25,000 g mol^{-1}) was purchased from abcr GmbH. 1,12-Dodecanediol dimethacrylate (DDDMA, CAS 72829-09-5) and Pentafluorophenyl acrylate (PFPA, CAS 71195-85-2) were acquired from TCI Europe N.V. The UV initiator 2,2-Dimethoxy-2-phenylacetophenone (Irgacure 651, CAS 24650-42-8) and all solvents were purchased from Sigma-Aldrich. Although commercially available, 2-((Trimethylsilyl)oxy)ethyl acrylate (TMS-HEA, CAS 18269-99-3) was synthesized according to previously reported procedures [34,67] and stored under argon at 4°C prior to use. Methacryloxytrimethylsilane (TMS-HEMA, CAS 17407-09-9) was synthesized.

4.2. Synthesis of APCNs

Different APCNs (Table 1) with varying phase ratios and different hydrophilic and hydrophobic precursors were synthesized. The hydrophilic precursors (TMS-HEA or a mixture of TMS-HEA with TMS-HEMA) were added to the hydrophobic precursors PDMS (~500 to 25,000 g mol^{-1}) or DDDMA with the initiator Irgacure 651. The acrylate PFPA was also tested. All samples were vortexed using a Vortex 3 shaker (IKA). PreAPCN films were fabricated between two glass microscopy slides using Tesa film stripes to achieve film thicknesses of around 200 μm, with a UVASPOT 400/T (Hoenle AG, Germany) applied for 3 min per side to polymerize the film. Following this, the films were swollen in acetone to detach the preAPCNs from the glass slides and then swollen in THF for 30 min to swell the hydrophobic phase as well. To remove the TMS group and create a biphasic network, the films were placed in a mixture of 1:1 H_2O: isopropanol acidified with HCl overnight. The APCN films were then swollen for 2h in THF for washing and to remove any residuals.

4.3. In-situ-strain-small angle X-ray scattering (SAXS)

Since conventional SAXS equipment was used during tensile testing, long exposure times were required to achieve good signal-to-noise ratios. The specimens were held at constant strain during the data acquisition process. Due to the viscoelastic behavior of both phases, both elongation and recovery took place during this time frame. The high flux of synchrotron radiation allowed one spectrum to be obtained within 1 s, meaning that real-time measurements could be made of the macroscopic mechanical properties and nanoscale deformations via SAXS. In-situ-strain-SAXS measurements were carried out using beamline I22 at Diamond Light Source Ltd (Didcot, Oxfordshire, UK). The instrument was equipped with 2 M Pilatus 2D detector (Dectris, Switzerland) and operated with an X-ray energy of 12.4 keV, enabling measurements of q values between 0.07 and 2 nm^{-1}, where q is the magnitude of the scattering vector and is defined by $q = \frac{4\pi}{\lambda}\sin(2\theta)$, and 2θ is the scattering angle. Serial SAXS images were recorded, each with an exposure time of 1s whereas a waiting time of 0.01s between each image were applied.

Whilst recording the serial SAXS images, the samples were subjected to tensile loading using a tensile stage TS 600 (Anton Paar GmbH, Graz, Austria) with a speed of 5 mm min^{-1} and a strain rate of 3.33×10^{-3} s^{-1}. For stress relaxation measurements the material was initially subjected to a stress of 0.56 MPa at a speed of 5 mm min^{-1} until a strain of 36% was reached. The rectangular sample was then held at this fixed strain while the stress decay was monitored. The APCN nanostructure during elongation and stress relaxation was simultaneously characterized by SAXS. This test measures how the stress gradually decreased over time while the APCNs were held at a constant strain. All samples were cut into rectangular strips of 5 mm width and 25 mm length.

The domain separations in APCNs could be well recognized by appearance of a ring in 2D SAXS patterns. In out APCN samples, the ring appeared around 0.2-0.8 nm^{-1}. As the sample is subjected to tensile stress, nanoscale deformation resulted in the transformation of the isotropic scattering ring into an ellipsoidal pattern, indicating anisotropic nanodomain formation. To quantitatively characterize these deformations, 1D SAXS profiles were extracted by azimuthal integration of the 2D patterns over 30° in the horizontal and vertical directions. Integrations performed on the left/right and top/bottom sides were averaged to improve statistics of 1D data. The scattering ring now appears as a peak in 1D profile which was fitted using a Lorentzian peak function combined with a Porod decay term, following the approach reported in our previous study [68].

The peak characteristics (peak position and peak broadness) were extracted to calculate the interdomain distance and domain sizes at both the vertical and horizontal directions; for unstretched samples, the peak positions at both directions are identical.

The sizes of the individual domains were calculated using Bragg equation $n\lambda = 2dsin(\theta)$, where n describes the order of the correlation peak, λ the wavelength of the incident X-ray beam, d the domain size and θ the scattering angle. The $d_{domain\ size}$ values were derived from the peak widths using the Scherrer equation $d_{inter\ distance} = \frac{\kappa\lambda}{\beta\ cos\ \theta}$, where κ is the shape factor, λ the X-ray wavelength, β the full width at half maximum (FWHM) and θ the Bragg angle.

The density of PDMS was taken as 0.98 g cm^{-3}, and the density of HEA was set to 1.083 g cm^{-3}.

$$d_{PDMS} = \frac{d_{inter\ distance}}{1 + \left(\frac{\omega\%_{HEA} * \rho_{PDMS}}{((100-\omega\%_{HEA}) * \rho_{HEA})^{1/3}}\right)} \quad (1)$$

The mapping experiments were performed by scanning a specimen that was stretched and held at 70% of its maximum elongation. The scan was conducted over an area of 13×3 mm^2 with a step size of 0.5 mm, resulting in a 6×26 measurement grid. Domain sizes in both the vertical and horizontal directions were then determined for each individual exposure by fitting the 1D SAXS as described above.

4.4. Tensile testing

Tensile tests following DIN 53505:2017-03 for MP00649 specimens were performed (except for sample 70PDMS50 (S3)) using a biaxial testing machine 4 × 100 N from ZwickRoell operated in uniaxial mode (class 1). The strain was measured with a video-extensometer with a resolution of 1 μm. The following mechanical properties were determined: tensile strength, Youngs's modulus, and elongation at break. A pre-load of 0.05 N and a speed of 1 mm min^{-1} were applied. Reports in the literature [35] indicate that the mechanical properties show little to no dependency on strain rate in APCNs containing HEA and PDMS, even at higher strain rates of up to 500 mm min^{-1}. Dogbone shaped specimens following DIN 53504:2009-10 were punched out from a membrane using a custom-made die, with nominal sample thicknesses of ~0.2 mm.

4.5. Dynamic Mechanical Thermal Analysis (DMTA)

In DMTA, the main parameters measured are the storage modulus E′, which represents the elastic (stored) energy in the material and thus indicating the polymer's stiffness. The T_g could be determined from the peaks in E" (red, Fig. 5c–e) and tan δ (blue, Fig. 5c–e). In an APCN, more energy is dissipated as the molecular motion increases, as indicated by peaks in the loss modulus E" and loss factor tan δ. A drop in the E' indicates the reduction in the stiffness of the material and its flexibility. In direct comparison to differential scanning calorimetry (DSC) the glass transitions derived from DMTA offer superior resolution. DSC measures the heat flux of a material during transitions. The resolution in DSCs can therefore be limited to detect transitions since the change in specific heat is lower [25,35] compared to the change in the mechanical behavior of the material as measured by DMTA. Dynamic temperature ramp tests were performed using the DMTA RSA III device (TA Instruments, New Castle, USA) in the tensile mode. The loss modulus E" represents the viscous energy, which is lost as heat. The loss factor tan δ describes the ratio of the loss modulus to the storage modulus E"/E′ and gives information about the relative degree of energy dissipation or damping (the polymer's ability to absorb energy). For samples 90PDMS50 (S1) to PFPA30_70PDMS50 (S6), tests were conducted over a temperature range of −135°C to 70°C or 100°C. A cooling rate of 5°C min^{-1} was applied when cooling down from room temperature to −135°C. Afterwards, a ramp rate of 2°C min^{-1} was set. The strain was set to 0.1% for temperatures when cooling down from room temperature to −135°C. Subsequently, a strain of 0.5% was applied when heating up to −10°C. Afterwards a strain of 1% was set until the end. For all samples the frequency was maintained at 1Hz.

Each sample was cut into rectangular films with dimensions of ~20 mm in length and ~6 mm in width.

4.6. Static Small angle X-ray scattering (SAXS)

Static SAXS measurements were performed on a Bruker NanoStar (Bruker AXS GmbH, Karlsruhe, Germany) at the Center for X-ray Analytics at Empa St. Gallen, Switzerland. X-rays were generated with a micro-focused Cu source (wavelength Cu K $\alpha = 1.5406$ Å). Scattering patterns were collected using a 2D MikroGap technology-based detector (VÅNTEC-500 2D) featuring 2048 x 2048 pixels with a size of 68×68 μm per pixel, together with a custom-built semi-transparent beam stop. The sample-to-detector distance was 107 cm. Measurements were performed at room temperature under a moderate vacuum of 10^{-2} mbar to minimize air scattering. SAXS data were analyzed using Sasfit software [69]. Fitting of the q values for the samples was carried out using a spinodal decomposing form factor and a 3D Hard Sphere structure factor. The scattering curve I (q) can be approximated with the following expression:

$$I(q) = I_{max} \frac{\left(1 + \frac{\gamma}{2}\right)\chi^2}{\frac{\gamma}{2} + \chi^2 + \gamma} \quad (2)$$

where $\chi = q/q_{max}$. The position of the correlation peak at q_{max} provides information about the size of the scattering structures and provides structural information of the scattering objects γ. γ is equal to 2D, where D represents the dimensionality of the scattering object. The fitted peak maxima in nm^{-1} were converted to inter distances d using the formula $d = 2\pi/q$. The respective sizes of the domains were calculated using equation (1).

4.7. Small-angle neutron scattering (SANS)

SANS measurements were carried out at SINQ (PSI) using the SANS-LLB instrument. Detector distances of 2.5, 6 and 18.3 m were used to cover a range of q-values from 0.025 to 0.25 nm with a neutron wavelength of $\lambda = 0.6$ nm. Solid films were loaded in Hellma QS110 cells with a 1 mm pathlength and soaked with deuterated solvent before the exposure to neutrons. The ambient temperature was 25°C. The scattering patterns were corrected for transmission, sample thickness, and dark and flat field and the intensity was brought to absolute scale using water for calibration.

4.8. Swelling measurements

All samples were dried in a VTR-5036 (Heraeus AG) vacuum drying oven at 60°C overnight to ensure complete moisture removal. The 1×1 cm samples were swollen in either distilled water or anhydrous toluene overnight at room temperature. The degree of swelling s_{grav} was calculated through gravimetric swelling tests, based on the assumption that each phase absorbed only the solvent with matching hydrophilicity.

$$S_{grav} = \frac{1}{n} \sum_{i=1}^{n} \left(m_{i,swollen} / m_{i,dry} \right) \quad (3)$$

4.9. Atomic force microscopy (AFM)

Elastic moduli were determined using AFM measurements on a Bruker Dimension with an ICON head (Bruker Corporation, Billerica, US) with ScanAsyst AIR probes (0.4 N/m, 70 kHz, Bruker Probes) in the force Volume Mode [70]. The samples were fixed onto an aluminum plate with double sided tape and a random spot was selected for each sample, for which 400 measurements were taken. The Johnson-Kendall-Roberts (JKR) contact mechanics model was used as a modulus fit model to analyze the acquired force curves.

CRediT authorship contribution statement

Hoai Maria Wolschner: Conceptualization, Formal analysis, Investigation, Methodology, Visualization, Writing – original draft. **Amin Sadeghpour:** Conceptualization, Formal analysis, Investigation, Methodology, Writing – review & editing. **Chieh-Szu Huang:** Conceptualization, Investigation, Methodology, Writing – review & editing. **Tina Künniger:** Investigation, Methodology, Writing – review & editing. **Bernhard Weisse:** Investigation, Methodology, Writing – review & editing. **Viviane Lutz-Bueno:** Investigation, Methodology, Writing – review & editing. **René M. Rossi:** Conceptualization, Funding acquisition, Supervision, Writing – review & editing. **Luciano F. Boesel:** Conceptualization, Funding acquisition, Methodology, Project administration, Supervision, Validation, Writing – review & editing.

Declaration of competing interests

The authors declare that they have no known competing financial interests.

Acknowledgement

We acknowledge Lea Oberhänsli for synthesizing TMS-HEA and TMS-HEMA; Empa's Center for X-ray Analytics and Jonathan Avaro for performing and providing us with the corresponding data analysis for the Static Small angle X-ray scattering (SAXS) measurements; access to the Scanning Probe Microscopy User Lab at Empa; and Michal Gora and Oleksandr Pshyk for support in finding a fitting method to determine the modulus via AFM. We acknowledge Diamond Light Source for time on I22 under proposal SM26958 and SM30847 and the beamline scientist Thomas Zinn and the Paul Scherrer Institute for allocation of beamtime in the SANS-LLB instrument. This work was supported by the Swiss Federal Office of Energy through grant number SI/502457-01 as well as by the Subitex research initiative (Switzerland).

Appendix B. Supplementary data

Supplementary data to this article can be found online at https://doi.org/10.1016/j.polymer.2026.130656.

Data availability

Data will be made available on request.

References

[1] C.S. Patrickios, T.K. Georgiou, Covalent amphiphilic polymer networks, Curr. Opin. Colloid Interface Sci. 8 (2003) 76–85, https://doi.org/10.1016/S1359-0294(03)00005-0.
[2] G. Erdodi, J.P. Kennedy, Amphiphilic conetworks: definition, synthesis, applications, Prog. Polym. Sci. 31 (2006) 1–18, https://doi.org/10.1016/j.progpolymsci.2005.11.001.
[3] C.S. Patrickios, K. Matyjaszewski, Amphiphilic polymer co-networks: 32 years old and growing stronger – a perspective, Polym. Int. 70 (2021) 10–13, https://doi.org/10.1002/pi.6138.
[4] K.F. Mueller, E.K. Kleiner, Polysiloxane Hydrogels, US4136250A, 1979. https://patents.google.com/patent/US4136250A/en. (Accessed 11 February 2026).
[5] C. Zhang, Z. Liu, H. Wang, X. Feng, C. He, Novel anti-biofouling soft contact lens: l-cysteine conjugated amphiphilic conetworks via RAFT and Thiol–Ene click chemistry, Macromol. Biosci. 17 (2017) 1600444, https://doi.org/10.1002/mabi.201600444.
[6] B. Kostova, K. Ivanova-Mileva, D. Rachev, D. Christova, Study of the potential of amphiphilic conetworks based on Poly(2-ethyl-2-oxazoline) as new platforms for delivery of drugs with limited solubility, AAPS PharmSciTech 14 (2013) 352–359, https://doi.org/10.1208/s12249-013-9923-7.
[7] K. Schöller, S. Küpfer, L. Baumann, P.M. Hoyer, D. de Courten, R.M. Rossi, A. Vetushka, M. Wolf, N. Bruns, L.J. Scherer, From membrane to skin: aqueous permeation control through light-responsive amphiphilic polymer Co-Networks, Adv. Funct. Mater. 24 (2014) 5194–5201, https://doi.org/10.1002/adfm.201400671.
[8] A.K.S. Chandel, C.U. Kumar, S.K. Jewrajka, Effect of polyethylene glycol on properties and drug encapsulation–release performance of biodegradable/

cytocompatible agarose–polyethylene glycol–polycaprolactone amphiphilic Co-Network gels, ACS Appl. Mater. Interfaces 8 (2016) 3182–3192, https://doi.org/10.1021/acsami.5b10675.
[9] Y.V. Cardona, L.G. Muñoz, D.G. Cardozo, A.F. Chamorro, Recent applications of amphiphilic copolymers in drug release systems for skin treatment, Pharmaceutics 16 (2024), https://doi.org/10.3390/pharmaceutics16091203.
[10] M. Hanko, N. Bruns, J.C. Tiller, J. Heinze, Optical biochemical sensor for determining hydroperoxides in nonpolar organic liquids as archetype for sensors consisting of amphiphilic conetworks as immobilisation matrices, Anal. Bioanal. Chem. 386 (2006) 1273–1283, https://doi.org/10.1007/s00216-006-0680-2.
[11] S. Meskath, J. Heinze, G. Urban, Silicone containing amphiphilic Co-Networks as immobilisation matrices for enzyme based biosensors: optochemical detection of gaseous hydrogen peroxide, EurosensorsXXV 25 (2011) 31–34, https://doi.org/10.1016/j.proeng.2011.12.008.
[12] S. Ulrich, A. Osypova, G. Panzarasa, R.M. Rossi, N. Bruns, L.F. Boesel, Pyranine-modified amphiphilic polymer conetworks as fluorescent ratiometric pH sensors, Macromol. Rapid Commun. 40 (2019) 1900360, https://doi.org/10.1002/marc.201900360.
[13] N. Bruns, J.C. Tiller, Amphiphilic network as nanoreactor for enzymes in organic solvents, Nano Lett. 5 (2005) 45–48, https://doi.org/10.1021/nl048413b.
[14] S. Dech, V. Wruk, C.P. Fik, J.C. Tiller, Amphiphilic polymer conetworks derived from aqueous solutions for biocatalysis in organic solvents, Polymer 53 (2012) 701–707, https://doi.org/10.1016/j.polymer.2011.12.027.
[15] D.E. Apostolides, G. Michael, C.S. Patrickios, B. Notredame, Y. Zhang, J.-F. Gohy, S. Prévost, M. Gradzielski, F.A. Jung, C.M. Papadakis, Dynamic covalent amphiphilic polymer conetworks based on end-linked pluronic F108: preparation, characterization, and evaluation as matrices for gel polymer electrolytes, ACS Appl. Mater. Interfaces 16 (2024) 23813–23825, https://doi.org/10.1021/acsami.3c19189.
[16] C.-S. Huang, K. Jakubowski, S. Ulrich, S. Yakunin, M. Clerc, C. Toncelli, R.M. Rossi, M.V. Kovalenko, L.F. Boesel, Nano-domains assisted energy transfer in amphiphilic polymer conetworks for wearable luminescent solar concentrators, Nano Energy 76 (2020) 105039, https://doi.org/10.1016/j.nanoen.2020.105039.
[17] C.-S. Huang, X. Kang, R.M. Rossi, M.V. Kovalenko, X. Sun, H. Peng, L.F. Boesel, Energy harvesting textiles: using wearable luminescent solar concentrators to improve the efficiency of fiber solar cells, J. Mater. Chem. A 9 (2021) 25974–25981, https://doi.org/10.1039/D1TA04984D.
[18] C.-S. Huang, S. Yakunin, J. Avaro, X. Kang, M.I. Bodnarchuk, M. Liebi, X. Sun, R. M. Rossi, M.V. Kovalenko, L.F. Boesel, Amphiphilic polymer co-network: a versatile matrix for tailoring the photonic energy transfer in wearable energy harvesting devices, Adv. Energy Mater. 12 (2022) 2200441, https://doi.org/10.1002/aenm.202200441.
[19] M. Rother, J. Barmettler, A. Reichmuth, J.V. Araujo, C. Rytka, O. Glaied, U. Pieles, N. Bruns, Self-sealing and puncture resistant breathable membranes for water-evaporation applications, Adv. Mater. 27 (2015) 6620–6624, https://doi.org/10.1002/adma.201502761.
[20] Z. Mutlu, S. Shams Es-haghi, M. Cakmak, Recent trends in advanced contact lenses, Adv. Healthc. Mater. 8 (2019) 1801390, https://doi.org/10.1002/adhm.201801390.
[21] D.G. Tsalikis, M. Ciobanu, C.S. Patrickios, Y. Higuchi, Model amphiphilic polymer conetworks in the bulk: dissipative particle dynamics simulations of their self-assembly and mechanical properties, Macromolecules 56 (2023) 9299–9311, https://doi.org/10.1021/acs.macromol.3c01392.
[22] S.T.R. Velasquez, D. Jang, J. Thomas, P. Grysan, L.T.J. Korley, N. Bruns, Advanced mechanical properties of amphiphilic polymer conetworks through hierarchical reinforcement with peptides and cellulose nanocrystals, Polym. Chem. 16 (2025) 2618–2628, https://doi.org/10.1039/D4PY01283F.
[23] D.E. Apostolides, G. Michael, K. Andronikou, C.S. Patrickios, S. Pásztor, G. Szarka, A. Petróczy, B. Iván, T. Sakai, S. Prévost, D.G. Tsalikis, M. Gradzielski, Synthesis of highly ordered amphiphilic polymer conetwork hydrogels via the topologically precise interconnection of two highly incompatible polymers, Chem. Mater. 37 (2025) 5515–5528, https://doi.org/10.1021/acs.chemmater.5c00127.
[24] M.P. Wolf, G.B. Salieb-Beugelaar, P. Hunziker, PDMS with designer functionalities—Properties, modifications strategies, and applications, Prog. Polym. Sci. 83 (2018) 97–134, https://doi.org/10.1016/j.progpolymsci.2018.06.001.
[25] S. Ulrich, A. Sadeghpour, R.M. Rossi, N. Bruns, L.F. Boesel, Wide range of functionalized Poly(N-alkyl acrylamide)-based amphiphilic polymer conetworks via active ester precursors, Macromolecules 51 (2018) 5267–5277, https://doi.org/10.1021/acs.macromol.8b00841.
[26] S. Castelletto, A. Boretti, Luminescence solar concentrators: a technology update, Nano Energy 109 (2023) 108269, https://doi.org/10.1016/j.nanoen.2023.108269.
[27] V. Prajzler, P. Nekvindova, J. Spirkova, M. Novotny, The evaluation of the refractive indices of bulk and thick polydimethylsiloxane and polydimethyl-diphenylsiloxane elastomers by the prism coupling technique, J. Mater. Sci. Mater. Electron. 28 (2017) 7951–7961, https://doi.org/10.1007/s10854-017-6498-1.
[28] J.C.R. Hernández, M.M. Pradas, J.L.G. Ribelles, Properties of poly(2-hydroxyethyl acrylate)-silica nanocomposites obtained by the sol–gel process, J. Non-Cryst. Solids 354 (2008) 1900–1908, https://doi.org/10.1016/j.jnoncrysol.2007.10.016.
[29] B. McKenna, R.C. Evans, Towards efficient spectral converters through materials design for luminescent solar devices, Adv. Mater. 29 (2017) 1606491, https://doi.org/10.1002/adma.201606491.
[30] M. Rafiee, S. Chandra, H. Ahmed, S.J. McCormack, An overview of various configurations of luminescent solar concentrators for photovoltaic applications, Opt. Mater. 91 (2019) 212–227, https://doi.org/10.1016/j.optmat.2019.01.007.
[31] R.W. Olson, R.F. Loring, M.D. Fayer, Luminescent solar concentrators and the reabsorption problem, Appl. Opt. 20 (1981) 2934–2940, https://doi.org/10.1364/AO.20.002934.
[32] B. Zhang, G. Lyu, E.A. Kelly, R.C. Evans, Förster resonance energy transfer in luminescent solar concentrators, Adv. Sci. 9 (2022) 2201160, https://doi.org/10.1002/advs.202201160.
[33] Th Förster, Zwischenmolekulare Energiewanderung und Fluoreszenz, Ann. Phys. 437 (1948) 55–75, https://doi.org/10.1002/andp.19484370105.
[34] N. Bruns, J. Scherble, L. Hartmann, R. Thomann, B. Iván, R. Mülhaupt, J.C. Tiller, Nanophase separated amphiphilic conetwork coatings and membranes, Macromolecules 38 (2005) 2431–2438, https://doi.org/10.1021/ma047302w.
[35] S.T.R. Velasquez, D. Jang, P. Jenkins, P. Liu, L. Yang, L.T.J. Korley, N. Bruns, Peptide-reinforced amphiphilic polymer conetworks, Adv. Funct. Mater. 32 (2022) 2207317, https://doi.org/10.1002/adfm.202207317.
[36] S.T.R. Velasquez, A. Belluati, E. Tervoort, I. Mattich, B. Hertel, S. Russell, M. G. Gouveia, P. Grysan, C. Mugemana, A.R. Studart, N. Bruns, Microfluidically produced microcapsules with amphiphilic polymer conetwork shells, Adv. Mater. Technol. 9 (2024) 2400109, https://doi.org/10.1002/admt.202400109.
[37] C.G. Wiener, C. Wang, Y. Liu, R.A. Weiss, B.D. Vogt, Nanostructure evolution during relaxation from a large step strain in a supramolecular copolymer-based hydrogel: a SANS investigation, Macromolecules 50 (2017) 1672–1680, https://doi.org/10.1021/acs.macromol.6b02680.
[38] K.L. Segura-Méndez, J.G. Puente-Córdova, F.Y. Rentería-Baltiérrez, J.F. Luna-Martínez, N. Mohamed-Noriega, Modeling of stress relaxation behavior in HDPE and PP using fractional derivatives, Polymers 17 (2025), https://doi.org/10.3390/polym17040453.
[39] C. Fodor, G. Kali, R. Thomann, Y. Thomann, B. Iván, R. Mülhaupt, Nanophasic morphologies as a function of the composition and molecular weight of the macromolecular cross-linker in poly(N-vinylimidazole)-l-poly(tetrahydrofuran) amphiphilic conetworks: bicontinuous domain structure in broad composition ranges, RSC Adv. 7 (2017) 6827–6834, https://doi.org/10.1039/C6RA25356C.
[40] S.A. Wilhelm, M. Maricanov, V. Brandt, F. Katzenberg, J.C. Tiller, Amphiphilic polymer conetworks with ideal and non-ideal swelling behavior demonstrated by small angle X-ray scattering, Polymer 242 (2022) 124582, https://doi.org/10.1016/j.polymer.2022.124582.
[41] P. Malo de Molina, D. Kafouris, C.S. Patrickios, L. Noirez, M. Gradzielski, Amphiphilic polymer conetworks studied by SANS: effect of the type of solubilizate and molecular architecture on the swollen gel structure, Macromolecules 56 (2023) 8323–8332, https://doi.org/10.1021/acs.macromol.3c01169.
[42] G.G. Ferrer, M.S. Sánchez, J.L.G. Ribelles, F.J.R. Colomer, M.M. Pradas, Nanodomains in a hydrophilic–hydrophobic IPN based on poly(2-hydroxyethyl acrylate) and poly(ethyl acrylate), Eur. Polym. J. 43 (2007) 3136–3145, https://doi.org/10.1016/j.eurpolymj.2007.05.019.
[43] J.A. Gómez Tejedor, T. Rodríguez Acosta, J.L. Gómez Ribelles, G. Polizos, P. Pissis, Poly(ethyl methacrylate-co-hydroxyethyl acrylate) random co-polymers: dielectric and dynamic-mechanical characterization, J. Non-Cryst. Solids 353 (2007) 276–285, https://doi.org/10.1016/j.jnoncrysol.2006.11.003.
[44] S. Utrera-Barrios, L. Yu, A.L. Skov, Revisiting the thermal transitions of polydimethylsiloxane (PDMS) elastomers: addressing common misconceptions with comprehensive data, Macromol. Mater. Eng. 310 (2025) 2500075, https://doi.org/10.1002/mame.202500075.
[45] A. Petróczy, I. Szanka, L. Bereczki, N. Hegyesi, J. Madarász, B. Iván, The scissors effect of the macromolecular crosslinker on the glass transition of polystyrene in its conetworks with poly(dimethylsiloxane), Polymers 17 (2025), https://doi.org/10.3390/polym17121656.
[46] I.M. Kalogeras, Glass-transition phenomena in polymer blends, in: Encycl. Polym. Blends, John Wiley & Sons, Ltd, 2016, pp. 1–134, https://doi.org/10.1002/9783527653966.ch1.
[47] G.D. Smith, D. Bedrov, Relationship between the α- and β-relaxation processes in amorphous polymers: insight from atomistic molecular dynamics simulations of 1,4-polybutadiene melts and blends, J. Polym. Sci., Part B: Polym. Phys. 45 (2007) 627–643, https://doi.org/10.1002/polb.21064.
[48] M. Asandulesa, V.E. Musteata, A. Bele, M. Dascalu, S. Bronnikov, C. Racles, Molecular dynamics of polysiloxane polar-nonpolar co-networks and blends studied by dielectric relaxation spectroscopy, Polymer 149 (2018) 73–84, https://doi.org/10.1016/j.polymer.2018.06.061.
[49] C. Fodor, A. Domján, B. Iván, Unprecedented scissor effect of macromolecular cross-linkers on the glass transition temperature of poly(N-vinylimidazole), crystallinity suppression of poly(tetrahydrofuran) and molecular mobility by solid state NMR in poly(N-vinylimidazole)-l-poly(tetrahydrofuran) conetworks, Polym. Chem. 4 (2013) 3714–3724, https://doi.org/10.1039/C3PY00299C.
[50] N.A. Peppas, H.J. Moynihan, L.M. Lucht, The structure of highly crosslinked poly (2-hydroxyethyl methacrylate) hydrogels, J. Biomed. Mater. Res. 19 (1985) 397–411, https://doi.org/10.1002/jbm.820190405.
[51] M.J. Schroeder, C.M. Roland, Segmental relaxation in end-linked Poly (dimethylsiloxane) networks, Macromolecules 35 (2002) 2676–2681, https://doi.org/10.1021/ma011678h.
[52] K. Sharma, W. Wang, S. Valet, T. Künniger, M. Góra, K. Wei, B. Weisse, L. Bahin, R. M. Rossi, F. Sorin, L.F. Boesel, Microfluidic wet spinning of soft polydimethylsiloxane polymer optical fibers, Mater. Des. 248 (2024) 113466, https://doi.org/10.1016/j.matdes.2024.113466.
[53] T.G. Fox, P.J. Flory, The glass temperature and related properties of polystyrene. Influence of molecular weight, J. Polym. Sci. 14 (1954) 315–319, https://doi.org/10.1002/pol.1954.120147514.

[54] C. Sinturel, F.S. Bates, M.A. Hillmyer, High χ–Low N block polymers: how far can we go? ACS Macro Lett. 4 (2015) 1044–1050, https://doi.org/10.1021/acsmacrolett.5b00472.
[55] F. Roussel, S. Saidi, F. Guittard, S. Geribaldi, Thermophysical properties of fluorinated acrylate homopolymers: mixing and phase separation, Eur. Phys. J. E 8 (2002) 283–288, https://doi.org/10.1140/epje/i2002-10014-4.
[56] R. Longenecker, T. Mu, M. Hanna, N.A.D. Burke, H.D.H. Stöver, Thermally responsive 2-Hydroxyethyl methacrylate polymers: soluble–insoluble and soluble–insoluble–soluble transitions, Macromolecules 44 (2011) 8962–8971, https://doi.org/10.1021/ma201528r.
[57] R.M. Arnold, C.D. McNitt, V.V. Popik, J. Locklin, Direct grafting of poly (pentafluorophenyl acrylate) onto oxides: versatile substrates for reactive microcapillary printing and self-sorting modification, Chem. Commun. 50 (2014) 5307–5309, https://doi.org/10.1039/C3CC47597B.
[58] X. Huang, S. Nakagawa, H. Houjou, N. Yoshie, Insights into the role of hydrogen bonds on the mechanical properties of polymer networks, Macromolecules 54 (2021) 4070–4080, https://doi.org/10.1021/acs.macromol.1c00120.
[59] P. Rajaee, I. Wijesinghe, Z. Li, C. Yan, Recent advances in polymeric materials with exceptional mechanical performance achieved via multiple hydrogen-bonded networks, RSC Appl. Polym. 3 (2025) 1428–1451, https://doi.org/10.1039/D5LP00189G.
[60] R. Tajima, S. Nakagawa, N. Yoshie, Multiple hydrogen bonds as tools to enhance the mechanical and mechanoresponsive properties of polymers, Polym. J. (2025), https://doi.org/10.1038/s41428-025-01098-6.
[61] G. Gebel, Structural evolution of water swollen perfluorosulfonated ionomers from dry membrane to solution, Polymer 41 (2000) 5829–5838, https://doi.org/10.1016/S0032-3861(99)00770-3.
[62] K. Hagmann, C. Schneider, S. Ihmann, F. Böhme, R. von Klitzing, Exploring structure-property relationship on a nanoscale for tailoring films of amphiphilic polymer Co-Networks, Macromol. Chem. Phys. 227 (2026) e00500, https://doi.org/10.1002/macp.202500500.
[63] V.N. Novikov, E.A. Rössler, Correlation between glass transition temperature and molecular mass in non-polymeric and polymer glass formers, Polymer 54 (2013) 6987–6991, https://doi.org/10.1016/j.polymer.2013.11.002.
[64] Physical Origin of the Mass Dependence of Glass Transition Temperature and Fragility of Polymer Liquids | Macromolecules, (n.d.). https://pubs.acs.org/doi/10.1021/acs.macromol.4c02991?_cf_chl_f_tk=zo4QBRgOZuJlaIbSe4y_pv4w2mhl2I.4.YGCkjsKGd8-1783174450-1.0.1.1-bXezBjzBpKjQvpaIDmsIVd6n.Uzi83Usdd_uvPsMtw (accessed July 4, 2026).
[65] M.P. Burdzy, D. Feng, K.J. Welch, Y. Wang, R.P. Cross, Curable elastomer compositions with low temperature sealing capability, WO2012149091A2, https://patents.google.com/patent/WO2012149091A2/en?oq=WO+2012%2f149091, 2012. (Accessed 4 February 2026).
[66] J.-D. Kouakou, M.A. Bangoura, R. Mérindol, K. Réhel, I. Linossier, G. Vignaud, F. Azemar, Influence of precursor molecular weight on swelling and elastic modulus of cross-linked PDMS films, Soft Matter 22 (2026) 508–517, https://doi.org/10.1039/D5SM00994D.
[67] J. Scherble, B. Iván, R. Mülhaupt, Online monitoring of silicone network formation by means of In-Situ mid-infrared spectroscopy, Macromol. Chem. Phys. 203 (2002) 1866–1871, https://doi.org/10.1002/1521-3935(200208)203:12<1866::AID-MACP1866>3.0.CO;2-G.
[68] A.K. Maurya, L. Weidenbacher, F. Spano, G. Fortunato, R.M. Rossi, M. Frenz, A. Dommann, A. Neels, A. Sadeghpour, Structural insights into semicrystalline states of electrospun nanofibers: a multiscale analytical approach, Nanoscale 11 (2019) 7176–7187, https://doi.org/10.1039/C9NR00446G.
[69] I. Breßler, J. Kohlbrecher, A.F. Thünemann, It SASfit: a tool for small-angle scattering data analysis using a library of analytical expressions, J. Appl. Crystallogr. 48 (2015) 1587–1598, https://doi.org/10.1107/S1600576715016544.
[70] M. Radmacher, M. Fritz, P.K. Hansma, Imaging soft samples with the atomic force microscope: gelatin in water and propanol, Biophys. J. 69 (1995) 264–270, https://doi.org/10.1016/S0006-3495(95)79897-6.